

Production characteristics of light nuclei, hypertritons and Ω -hypernuclei in Pb+Pb collisions at $\sqrt{s_{NN}} = 5.02$ TeV

Rui-Qin Wang,^{1,*} Xin-Lei Hou,¹ Yan-Hao Li,¹ Jun Song,^{2,†} and Feng-Lan Shao^{1,‡}

¹*School of Physics and Physical Engineering, Qufu Normal University, Shandong 273165, China*

²*School of Physical Science and Intelligent Engineering, Jining University, Shandong 273155, China*

We extend an analytical nucleon coalescence model with hyperons to study productions of light nuclei, hypertritons and Ω -hypernuclei in Pb+Pb collisions at $\sqrt{s_{NN}} = 5.02$ TeV. We derive the formula of the momentum distribution of two bodies coalescing into dibaryon states and that of three bodies coalescing into tribaryon states. We explain the available data of the coalescence factors B_2 and B_3 , the transverse momentum spectra, the averaged transverse momenta, the yield rapidity densities, yield ratios of the deuteron, antihelium-3, antitriton, hypertriton measured by the ALICE collaboration, and give predictions of different Ω -hypernuclei, e.g., $H(p\Omega^-)$, $H(n\Omega^-)$ and $H(pn\Omega^-)$. We find two groups of interesting observables, the averaged transverse momentum ratios of light (hyper-)nuclei to protons (hyperons) and the centrality-dependent yield ratios of theirs. The former group exhibits a reverse-hierarchy of the nucleus size, and the latter is helpful for the judgements of the nucleus production mechanism as well as the nucleus own size.

PACS numbers: 25.75.-q, 25.75.Dw, 27.10.+h, 21.80.+a

I. INTRODUCTION

In ultra-relativistic heavy ion collisions, light nuclei and hypernuclei such as the deuteron (d), helium-3 (${}^3\text{He}$), triton (t), hypertriton (${}^3_\Lambda\text{H}$) and helium-4 (${}^4\text{He}$) are a special group of observables [1–13]. They are composite clusters and their production mechanism is currently still under debate. The productions of such composite objects closely relate with many fundamental issues in relativistic heavy ion collision physics, e.g., the hadronization mechanism [3], the structure of the quantum chromodynamics phase diagram [4–8], the local baryon-strangeness correlation [9], the hyperon-nucleon interaction [10, 11] and the search of more hadronic molecular states [12, 13].

In recent decades, the production of light nuclei and hypernuclei in ultra-relativistic heavy ion collisions has always attracted much attention both in experiment [14–26] and in theory [27–33]. The STAR experiment at the BNL Relativistic Heavy Ion Collider (RHIC) and the ALICE experiment at the CERN Large Hadron Collider (LHC) have put many efforts on measurements of light nuclei [17–22] and hypernuclei [23–26]. In theory two production mechanisms, the thermal production mechanism [33–37] and the coalescence mechanism [31, 32, 38–46], have proved to be successful in describing formations of such composite objects.

The coalescence mechanism, in which light nuclei and hypernuclei are assumed to be produced by the coalescence of the adjacent nucleons and hyperons in the phase space, possesses some unique characteristics. In order to see whether, if so, to what extent, these characteristics depend on the particular coalescence models used in obtaining these characteristics, we in our previous works [47–50] developed an analytical description for the production of different species of light

nuclei. We applied the analytical nucleon coalescence model to Au+Au collisions at the RHIC to successfully explain the energy-dependent behaviors of d , t , ${}^3\text{He}$ and ${}^4\text{He}$ [47, 48]. We also applied it to pp, p+Pb and Pb+Pb collisions at the LHC to understand the different behaviors of the coalescence factors B_2 and B_3 [49] from small to large collision systems, and gave a series of concise production correlations of d , ${}^3\text{He}$ and t [50].

Very recently, the ALICE collaboration published the most precise measurements to date of d , ${}^3\text{He}$, t and especially ${}^3_\Lambda\text{H}$ in Pb+Pb collisions at $\sqrt{s_{NN}} = 5.02$ TeV [22, 25, 51]. In this work, we extend the coalescence model considering the coordinate-momentum correlation [50] to include the hyperon coalescence besides the nucleon coalescence, and apply it to simultaneously study productions of light nuclei, the ${}^3_\Lambda\text{H}$ and different Ω -hypernuclei. One main goal of this article is to give an overall comprehension for the newest data in Pb+Pb collisions with the highest collision energy up to now. The other goal is to bring production characteristics of light nuclei and hypernuclei originating from the coalescence itself to light.

The paper is organized as follows. In Sec. II, we give an introduction to the coalescence model. We present the formula of the momentum distribution of two baryons coalescing into dibaryon states and that of three baryons coalescing into tribaryon states. In Sec. III, we study behaviors of the coalescence factors B_2 and B_3 as functions of the collision centrality and the transverse momentum per nucleon. We also study the transverse momentum (p_T) spectra, the averaged transverse momenta $\langle p_T \rangle$, the yield rapidity densities dN/dy and yield ratios of d , ${}^3\text{He}$ and t . In Sec. IV, we present results of the ${}^3_\Lambda\text{H}$ and Ω -hypernuclei. We specially study the averaged transverse momentum ratios $\langle p_T \rangle_d / \langle p_T \rangle_p$, $\langle p_T \rangle_{H(p\Omega^-)} / \langle p_T \rangle_{\Omega^-}$, $\langle p_T \rangle_{H(n\Omega^-)} / \langle p_T \rangle_{\Omega^-}$, $\langle p_T \rangle_t / \langle p_T \rangle_p$, $\langle p_T \rangle_{{}^3\text{He}} / \langle p_T \rangle_p$, $\langle p_T \rangle_{{}^3_\Lambda\text{H}} / \langle p_T \rangle_\Lambda$, $\langle p_T \rangle_{H(pn\Omega^-)} / \langle p_T \rangle_{\Omega^-}$, and centrality-dependent behaviors of yield ratios d/p , $H(p\Omega^-)/\Omega^-$, $H(n\Omega^-)/\Omega^-$, t/p , ${}^3\text{He}/p$, ${}^3_\Lambda\text{H}/\Lambda$, $H(pn\Omega^-)/\Omega^-$. In Sec. V, we give our summary.

* wangrq@qfnu.edu.cn

† songjun2011@jnxu.edu.cn

‡ shaofl@mail.sdu.edu.cn

II. THE COALESCENCE MODEL

In this section we extend the analytical nucleon coalescence model in our previous work [50] to include the coalescence of hyperons. In the current coalescence model, the coalescence process is executed on an equivalent kinetic freeze-out surface formed from different times. To make the analytical and intuitive insights possible, we abandon carrying out the time evolution step by step but absorb the finite emission duration in an effective volume parameter. We first present the formalism of two baryons coalescing into d -like dibaryon states. We then give analytical expressions of three baryons coalescing into ${}^3\text{He}$, t and their partners in the strange sector.

A. Formalism of two bodies coalescing into dibaryon states

We begin with a hadronic system produced at the final stage of the evolution of high energy collision and suppose the dibaryon state H_j is formed via the coalescence of two baryons h_1 and h_2 . We use $f_{H_j}(\mathbf{p})$ to denote the three-dimensional momentum distribution of the produced H_j and it is given by

$$f_{H_j}(\mathbf{p}) = \int d\mathbf{x}_1 d\mathbf{x}_2 d\mathbf{p}_1 d\mathbf{p}_2 f_{h_1 h_2}(\mathbf{x}_1, \mathbf{x}_2; \mathbf{p}_1, \mathbf{p}_2) \times \mathcal{R}_{H_j}(\mathbf{x}_1, \mathbf{x}_2; \mathbf{p}_1, \mathbf{p}_2, \mathbf{p}), \quad (1)$$

where $f_{h_1 h_2}(\mathbf{x}_1, \mathbf{x}_2; \mathbf{p}_1, \mathbf{p}_2)$ is two-baryon joint coordinate-momentum distribution; $\mathcal{R}_{H_j}(\mathbf{x}_1, \mathbf{x}_2; \mathbf{p}_1, \mathbf{p}_2, \mathbf{p})$ is the kernel function of the H_j . Here and from now on we use bold symbols to denote three-dimensional coordinate or momentum vectors.

In terms of the normalized joint coordinate-momentum distribution denoted by the superscript ‘(n)’, we have

$$f_{H_j}(\mathbf{p}) = N_{h_1 h_2} \int d\mathbf{x}_1 d\mathbf{x}_2 d\mathbf{p}_1 d\mathbf{p}_2 f_{h_1 h_2}^{(n)}(\mathbf{x}_1, \mathbf{x}_2; \mathbf{p}_1, \mathbf{p}_2) \times \mathcal{R}_{H_j}(\mathbf{x}_1, \mathbf{x}_2; \mathbf{p}_1, \mathbf{p}_2, \mathbf{p}). \quad (2)$$

$N_{h_1 h_2} = N_{h_1} N_{h_2}$ is the number of all possible $h_1 h_2$ -pairs in the considered hadronic system, and N_{h_i} ($i = 1, 2$) is the number of the baryons h_i .

The kernel function $\mathcal{R}_{H_j}(\mathbf{x}_1, \mathbf{x}_2; \mathbf{p}_1, \mathbf{p}_2, \mathbf{p})$ denotes the probability density for h_1, h_2 with momenta \mathbf{p}_1 and \mathbf{p}_2 at \mathbf{x}_1 and \mathbf{x}_2 to combine into an H_j of momentum \mathbf{p} . It carries the kinetic and dynamical information of h_1 and h_2 combining into H_j , and its precise expression should be constrained by such as the momentum conservation, constraints due to intrinsic quantum numbers e.g., spin [47–50]. To take these constraints into account explicitly, we rewrite the kernel function in the following form

$$\mathcal{R}_{H_j}(\mathbf{x}_1, \mathbf{x}_2; \mathbf{p}_1, \mathbf{p}_2, \mathbf{p}) = g_{H_j} \mathcal{R}_{H_j}^{(x,p)}(\mathbf{x}_1, \mathbf{x}_2; \mathbf{p}_1, \mathbf{p}_2) \delta\left(\sum_{i=1}^2 \mathbf{p}_i - \mathbf{p}\right) \quad (3)$$

The spin degeneracy factor $g_{H_j} = (2J_{H_j} + 1) / [\prod_{i=1}^2 (2J_{h_i} + 1)]$, where J_{H_j} is the spin of the produced H_j and J_{h_i} is that of

the primordial baryon h_i . The Dirac δ function guarantees the momentum conservation in the coalescence process. The remaining $\mathcal{R}_{H_j}^{(x,p)}(\mathbf{x}_1, \mathbf{x}_2; \mathbf{p}_1, \mathbf{p}_2)$ can be solved from the Wigner transformation as the H_j wave function is given. Considering the wave function of a spherical harmonic oscillator is particularly tractable and useful for analytical insight, we adopt this profile as in Refs. [52, 53] and have

$$\mathcal{R}_{H_j}^{(x,p)}(\mathbf{x}_1, \mathbf{x}_2; \mathbf{p}_1, \mathbf{p}_2) = 8e^{-\frac{(\mathbf{x}'_1 - \mathbf{x}'_2)^2}{2\sigma^2}} e^{-\frac{2\sigma^2(m_2 \mathbf{p}'_1 - m_1 \mathbf{p}'_2)^2}{(m_1 + m_2)^2 \hbar^2 c^2}}. \quad (4)$$

The superscript ‘’ in the coordinate or momentum variable denotes the baryon coordinate or momentum in the rest frame of the $h_1 h_2$ -pair. m_1 and m_2 are the mass of h_1 and that of h_2 . The width parameter $\sigma = \sqrt{\frac{2(m_1 + m_2)^2}{3(m_1^2 + m_2^2)}} R_{H_j}$, where R_{H_j} is the root-mean-square radius of H_j . The factor $\hbar c$ comes from the used GeVfm unit, and it is 0.197 GeVfm.

Substituting Eqs. (3) and (4) into Eq. (2), we have

$$f_{H_j}(\mathbf{p}) = N_{h_1 h_2} g_{H_j} \int d\mathbf{x}_1 d\mathbf{x}_2 d\mathbf{p}_1 d\mathbf{p}_2 f_{h_1 h_2}^{(n)}(\mathbf{x}_1, \mathbf{x}_2; \mathbf{p}_1, \mathbf{p}_2) \times 8e^{-\frac{(\mathbf{x}'_1 - \mathbf{x}'_2)^2}{2\sigma^2}} e^{-\frac{2\sigma^2(m_2 \mathbf{p}'_1 - m_1 \mathbf{p}'_2)^2}{(m_1 + m_2)^2 \hbar^2 c^2}} \delta\left(\sum_{i=1}^2 \mathbf{p}_i - \mathbf{p}\right). \quad (5)$$

This is the general formalism of the H_j produced via the coalescence of two baryons h_1 and h_2 .

Noticing that the root-mean-square radius R_{H_j} of the d -like dibaryon state H_j is always considered to be about or larger than 2 fm, σ is even larger than R_{H_j} . So the gaussian width in the momentum-dependent part of the kernel function in Eq. (5) has a small value, about or smaller than 0.1 GeV. Therefore, we approximate the gaussian form of the momentum-dependent kernel function to be a δ function form as follows

$$e^{-\frac{(\mathbf{p}'_1 - \frac{m_1}{m_2} \mathbf{p}'_2)^2}{(1 + \frac{m_1}{m_2})^2 \frac{\hbar^2 c^2}{2\sigma^2}}} \approx \left[\frac{\hbar c}{\sigma} \left(1 + \frac{m_1}{m_2}\right) \sqrt{\frac{\pi}{2}} \right]^3 \delta\left(\mathbf{p}'_1 - \frac{m_1}{m_2} \mathbf{p}'_2\right). \quad (6)$$

Substituting Eq. (6) into Eq. (5) and integrating \mathbf{p}_1 and \mathbf{p}_2 , we can obtain

$$\begin{aligned} f_{H_j}(\mathbf{p}) &= 8g_{H_j} N_{h_1 h_2} \int d\mathbf{x}_1 d\mathbf{x}_2 d\mathbf{p}_1 d\mathbf{p}_2 f_{h_1 h_2}^{(n)}(\mathbf{x}_1, \mathbf{x}_2; \mathbf{p}_1, \mathbf{p}_2) \\ &\times e^{-\frac{(\mathbf{x}'_1 - \mathbf{x}'_2)^2}{2\sigma^2}} \left(\frac{\hbar c \sqrt{\pi}}{\sqrt{2}\sigma}\right)^3 \left(1 + \frac{m_1}{m_2}\right)^3 \delta\left(\mathbf{p}'_1 - \frac{m_1}{m_2} \mathbf{p}'_2\right) \delta\left(\sum_{i=1}^2 \mathbf{p}_i - \mathbf{p}\right) \\ &= 8g_{H_j} N_{h_1 h_2} \int d\mathbf{x}_1 d\mathbf{x}_2 d\mathbf{p}_1 d\mathbf{p}_2 f_{h_1 h_2}^{(n)}(\mathbf{x}_1, \mathbf{x}_2; \mathbf{p}_1, \mathbf{p}_2) \\ &\times e^{-\frac{(\mathbf{x}'_1 - \mathbf{x}'_2)^2}{2\sigma^2}} \left(\frac{\hbar c \sqrt{\pi}}{\sqrt{2}\sigma}\right)^3 \left(1 + \frac{m_1}{m_2}\right)^3 \gamma \delta\left(\mathbf{p}_1 - \frac{m_1}{m_2} \mathbf{p}_2\right) \delta\left(\sum_{i=1}^2 \mathbf{p}_i - \mathbf{p}\right) \\ &= 8g_{H_j} N_{h_1 h_2} \gamma \left(\frac{\hbar c \sqrt{\pi}}{\sqrt{2}\sigma}\right)^3 \\ &\times \int d\mathbf{x}_1 d\mathbf{x}_2 f_{h_1 h_2}^{(n)}(\mathbf{x}_1, \mathbf{x}_2; \frac{m_1 \mathbf{p}}{m_1 + m_2}, \frac{m_2 \mathbf{p}}{m_1 + m_2}) e^{-\frac{(\mathbf{x}'_1 - \mathbf{x}'_2)^2}{2\sigma^2}}, \quad (7) \end{aligned}$$

where γ comes from the Lorentz transformation $\mathbf{p}'_1 - \frac{m_1}{m_2} \mathbf{p}'_2 = \frac{1}{\gamma} (\mathbf{p}_1 - \frac{m_1}{m_2} \mathbf{p}_2)$.

Changing coordinate variables in Eq. (7) to be $\mathbf{X} = \frac{\mathbf{x}_1 + \mathbf{x}_2}{\sqrt{2}}$ and $\mathbf{r} = \frac{\mathbf{x}_1 - \mathbf{x}_2}{\sqrt{2}}$, we have

$$f_{H_j}(\mathbf{p}) = 8g_{H_j}N_{h_1h_2} \left(\frac{\hbar c \sqrt{\pi}}{\sqrt{2}\sigma} \right)^3 \gamma \times \int d\mathbf{X} d\mathbf{r} f_{h_1h_2}^{(n)} \left(\mathbf{X}, \mathbf{r}; \frac{m_1}{m_1+m_2} \mathbf{p}, \frac{m_2}{m_1+m_2} \mathbf{p} \right) e^{-\frac{r^2}{\sigma^2}}. \quad (8)$$

Considering the strong interaction and the coalescence are local, we neglect the effect of collective motion on the center of mass coordinate and assume it is factorized, i.e.,

$$f_{h_1h_2}^{(n)} \left(\mathbf{X}, \mathbf{r}; \frac{m_1}{m_1+m_2} \mathbf{p}, \frac{m_2}{m_1+m_2} \mathbf{p} \right) = f_{h_1h_2}^{(n)}(\mathbf{X}) \times f_{h_1h_2}^{(n)} \left(\mathbf{r}; \frac{m_1}{m_1+m_2} \mathbf{p}, \frac{m_2}{m_1+m_2} \mathbf{p} \right). \quad (9)$$

Substituting Eq. (9) into Eq. (8), we have

$$f_{H_j}(\mathbf{p}) = 8g_{H_j}N_{h_1h_2} \left(\frac{\hbar c \sqrt{\pi}}{\sqrt{2}\sigma} \right)^3 \gamma \times \int d\mathbf{r} f_{h_1h_2}^{(n)} \left(\mathbf{r}; \frac{m_1}{m_1+m_2} \mathbf{p}, \frac{m_2}{m_1+m_2} \mathbf{p} \right) e^{-\frac{r^2}{\sigma^2}}. \quad (10)$$

We adopt the frequently-used gaussian form for the relative coordinate distribution as in such as Ref. [54], i.e.,

$$f_{h_1h_2}^{(n)} \left(\mathbf{r}; \frac{m_1}{m_1+m_2} \mathbf{p}, \frac{m_2}{m_1+m_2} \mathbf{p} \right) = \frac{1}{[\pi C_w R_f^2(\mathbf{p})]^{3/2}} e^{-\frac{r^2}{C_w R_f^2(\mathbf{p})}} \times f_{h_1h_2}^{(n)} \left(\frac{m_1}{m_1+m_2} \mathbf{p}, \frac{m_2}{m_1+m_2} \mathbf{p} \right). \quad (11)$$

Here $R_f(\mathbf{p})$ is the effective radius of the hadronic source system at the H_j freeze-out. C_w is a distribution width parameter and it is 2 [54]. Gaussian profile of the relative coordinate distribution is convenient for analytical calculations, and there are some empirical arguments in favor of such choice [55, 56].

With instantaneous coalescence in the rest frame of h_1h_2 -pair, i.e., $\Delta t' = 0$, we get the Lorentz transformation

$$\mathbf{r} = \mathbf{r}' + (\gamma - 1) \frac{\mathbf{r}' \cdot \boldsymbol{\beta}}{\beta^2} \boldsymbol{\beta}, \quad (12)$$

where $\boldsymbol{\beta}$ is the three-dimensional velocity vector of the center-of-mass frame of h_1h_2 -pair in the laboratory frame and γ is the corresponding contraction factor. Substituting Eq. (11) into Eq. (10) and using Eq. (12) to integrate from the relative coordinate variable, we obtain

$$f_{H_j}(\mathbf{p}) = \frac{(\sqrt{2\pi}\hbar c)^3 g_{H_j} \gamma}{[C_w R_f^2(\mathbf{p}) + \sigma^2] \sqrt{C_w [R_f(\mathbf{p})/\gamma]^2 + \sigma^2}} \times f_{h_1h_2} \left(\frac{m_1}{m_1+m_2} \mathbf{p}, \frac{m_2}{m_1+m_2} \mathbf{p} \right). \quad (13)$$

Ignoring correlations between h_1 and h_2 , we have the three-dimensional momentum distribution of the H_j as

$$f_{H_j}(\mathbf{p}) = \frac{(\sqrt{2\pi}\hbar c)^3 g_{H_j} \gamma}{[C_w R_f^2(\mathbf{p}) + \sigma^2] \sqrt{C_w [R_f(\mathbf{p})/\gamma]^2 + \sigma^2}} \times f_{h_1} \left(\frac{m_1 \mathbf{p}}{m_1+m_2} \right) f_{h_2} \left(\frac{m_2 \mathbf{p}}{m_1+m_2} \right). \quad (14)$$

Denoting the Lorentz invariant momentum distribution $\frac{d^2N}{2\pi p_T dp_T dy}$ with $f^{(inv)}$, we finally have

$$f_{H_j}^{(inv)}(p_T, y) = \frac{(\sqrt{2\pi}\hbar c)^3 g_{H_j}}{[C_w R_f^2(p_T, y) + \sigma^2] \sqrt{C_w [R_f(p_T, y)/\gamma]^2 + \sigma^2}} \times \frac{m_{H_j}}{m_1 m_2} f_{h_1}^{(inv)} \left(\frac{m_1 p_T}{m_1+m_2}, y \right) f_{h_2}^{(inv)} \left(\frac{m_2 p_T}{m_1+m_2}, y \right), \quad (15)$$

where y is the longitudinal rapidity and m_{H_j} is the mass of the H_j .

B. Formalism of three bodies coalescing into tribaryon states

For tribaryon state H_j formed via the coalescence of three baryons h_1 , h_2 and h_3 , the momentum distribution $f_{H_j}(\mathbf{p})$ is

$$f_{H_j}(\mathbf{p}) = N_{h_1h_2h_3} \times \int d\mathbf{x}_1 d\mathbf{x}_2 d\mathbf{x}_3 d\mathbf{p}_1 d\mathbf{p}_2 d\mathbf{p}_3 f_{h_1h_2h_3}^{(n)}(\mathbf{x}_1, \mathbf{x}_2, \mathbf{x}_3; \mathbf{p}_1, \mathbf{p}_2, \mathbf{p}_3) \times \mathcal{R}_{H_j}(\mathbf{x}_1, \mathbf{x}_2, \mathbf{x}_3; \mathbf{p}_1, \mathbf{p}_2, \mathbf{p}_3, \mathbf{p}). \quad (16)$$

$N_{h_1h_2h_3}$ is the number of all possible $h_1h_2h_3$ -clusters and it equals to $N_{h_1}N_{h_2}N_{h_3}$, $N_{h_1}(N_{h_1}-1)N_{h_3}$ for $h_1 \neq h_2 \neq h_3$, $h_1 = h_2 \neq h_3$, respectively. $f_{h_1h_2h_3}^{(n)}(\mathbf{x}_1, \mathbf{x}_2, \mathbf{x}_3; \mathbf{p}_1, \mathbf{p}_2, \mathbf{p}_3)$ is the normalized three-baryon joint coordinate-momentum distribution. $\mathcal{R}_{H_j}(\mathbf{x}_1, \mathbf{x}_2, \mathbf{x}_3; \mathbf{p}_1, \mathbf{p}_2, \mathbf{p}_3, \mathbf{p})$ is the kernel function.

We rewrite the kernel function as

$$\mathcal{R}_{H_j}(\mathbf{x}_1, \mathbf{x}_2, \mathbf{x}_3; \mathbf{p}_1, \mathbf{p}_2, \mathbf{p}_3, \mathbf{p}) = g_{H_j} \mathcal{R}_{H_j}^{(x,p)}(\mathbf{x}_1, \mathbf{x}_2, \mathbf{x}_3; \mathbf{p}_1, \mathbf{p}_2, \mathbf{p}_3) \times \delta \left(\sum_{i=1}^3 \mathbf{p}_i - \mathbf{p} \right). \quad (17)$$

The spin degeneracy factor $g_{H_j} = (2J_{H_j} + 1)/[\prod_{i=1}^3 (2J_{h_i} + 1)]$.

The Dirac δ function guarantees the momentum conservation. $\mathcal{R}_{H_j}^{(x,p)}(\mathbf{x}_1, \mathbf{x}_2, \mathbf{x}_3; \mathbf{p}_1, \mathbf{p}_2, \mathbf{p}_3)$ solving from the Wigner transformation [52, 53] is

$$\mathcal{R}_{H_j}^{(x,p)}(\mathbf{x}_1, \mathbf{x}_2, \mathbf{x}_3; \mathbf{p}_1, \mathbf{p}_2, \mathbf{p}_3) = 8^2 e^{-\frac{(\mathbf{x}'_1 - \mathbf{x}'_2)^2}{2\sigma_1^2}} e^{-\frac{2(\frac{m_1 \mathbf{x}'_1}{m_1+m_2} + \frac{m_2 \mathbf{x}'_2}{m_1+m_2} - \mathbf{x}'_3)^2}{3\sigma_2^2}} \times e^{-\frac{2\sigma_1^2(m_2 \mathbf{p}'_1 - m_1 \mathbf{p}'_2)^2}{(m_1+m_2)^2 \hbar^2 c^2}} e^{-\frac{3\sigma_2^2[m_3 \mathbf{p}'_1 + m_3 \mathbf{p}'_2 - (m_1+m_2) \mathbf{p}'_3]^2}{2(m_1+m_2+m_3)^2 \hbar^2 c^2}}. \quad (18)$$

The superscript “ $'$ ” denotes the baryon coordinate or momentum in the rest frame of the $h_1h_2h_3$ -cluster. The width parameter $\sigma_1 = \sqrt{\frac{m_3(m_1+m_2)(m_1+m_2+m_3)}{m_1m_2(m_1+m_2)+m_2m_3(m_2+m_3)+m_3m_1(m_3+m_1)}} R_{H_j}$, and

$$\sigma_2 = \sqrt{\frac{4m_1m_2(m_1+m_2+m_3)^2}{3(m_1+m_2)[m_1m_2(m_1+m_2)+m_2m_3(m_2+m_3)+m_3m_1(m_3+m_1)]}} R_{H_j}.$$

Substituting Eqs. (17) and (18) into Eq. (16), we have

$$f_{H_j}(\mathbf{p}) = 8^2 N_{h_1 h_2 h_3} g_{H_j} \int d\mathbf{x}_1 d\mathbf{x}_2 d\mathbf{x}_3 d\mathbf{p}_1 d\mathbf{p}_2 d\mathbf{p}_3 e^{-\frac{(\mathbf{x}'_1 - \mathbf{x}'_2)^2}{2\sigma_1^2}} \times e^{-\frac{2(\frac{m_1 \mathbf{x}'_1}{m_1+m_2} + \frac{m_2 \mathbf{x}'_2}{m_1+m_2} - \mathbf{x}'_3)^2}{3\sigma_2^2}} f_{h_1 h_2 h_3}^{(n)}(\mathbf{x}_1, \mathbf{x}_2, \mathbf{x}_3; \mathbf{p}_1, \mathbf{p}_2, \mathbf{p}_3)$$

$$\times e^{-\frac{2\sigma_1^2(m_2 \mathbf{p}'_1 - m_1 \mathbf{p}'_2)^2}{(m_1+m_2)^2 \hbar^2 c^2}} e^{-\frac{3\sigma_2^2[m_3 \mathbf{p}'_1 + m_3 \mathbf{p}'_2 - (m_1+m_2)\mathbf{p}'_3]^2}{2(m_1+m_2+m_3)^2 \hbar^2 c^2}} \delta(\sum_{i=1}^3 \mathbf{p}_i - \mathbf{p}). \quad (19)$$

Approximating the gaussian form of the momentum-dependent kernel function to be δ function form and integrating \mathbf{p}_1 , \mathbf{p}_2 and \mathbf{p}_3 from Eq. (19), we can obtain

$$\begin{aligned} f_{H_j}(\mathbf{p}) &= 8^2 N_{h_1 h_2 h_3} g_{H_j} \int d\mathbf{x}_1 d\mathbf{x}_2 d\mathbf{x}_3 d\mathbf{p}_1 d\mathbf{p}_2 d\mathbf{p}_3 f_{h_1 h_2 h_3}^{(n)}(\mathbf{x}_1, \mathbf{x}_2, \mathbf{x}_3; \mathbf{p}_1, \mathbf{p}_2, \mathbf{p}_3) e^{-\frac{(\mathbf{x}'_1 - \mathbf{x}'_2)^2}{2\sigma_1^2}} e^{-\frac{2(\frac{m_1 \mathbf{x}'_1}{m_1+m_2} + \frac{m_2 \mathbf{x}'_2}{m_1+m_2} - \mathbf{x}'_3)^2}{3\sigma_2^2}} \\ &\times \left(\frac{\hbar c \sqrt{\pi}}{\sqrt{2}\sigma_1}\right)^3 \left(1 + \frac{m_1}{m_2}\right)^3 \delta(\mathbf{p}'_1 - \frac{m_1}{m_2} \mathbf{p}'_2) \left(\frac{\sqrt{2}\pi\hbar c}{\sqrt{3}\sigma_2}\right)^3 \left(1 + \frac{m_1}{m_3} + \frac{m_2}{m_3}\right)^3 \delta(\mathbf{p}'_1 + \mathbf{p}'_2 - \frac{m_1+m_2}{m_3} \mathbf{p}'_3) \delta(\sum_{i=1}^2 \mathbf{p}_i - \mathbf{p}) \\ &= 8^2 N_{h_1 h_2 h_3} g_{H_j} \int d\mathbf{x}_1 d\mathbf{x}_2 d\mathbf{x}_3 d\mathbf{p}_1 d\mathbf{p}_2 d\mathbf{p}_3 f_{h_1 h_2 h_3}^{(n)}(\mathbf{x}_1, \mathbf{x}_2, \mathbf{x}_3; \mathbf{p}_1, \mathbf{p}_2, \mathbf{p}_3) e^{-\frac{(\mathbf{x}'_1 - \mathbf{x}'_2)^2}{2\sigma_1^2}} e^{-\frac{2(\frac{m_1 \mathbf{x}'_1}{m_1+m_2} + \frac{m_2 \mathbf{x}'_2}{m_1+m_2} - \mathbf{x}'_3)^2}{3\sigma_2^2}} \\ &\times \left(\frac{\hbar c \sqrt{\pi}}{\sqrt{2}\sigma_1}\right)^3 \left(1 + \frac{m_1}{m_2}\right)^3 \gamma \delta(\mathbf{p}_1 - \frac{m_1}{m_2} \mathbf{p}_2) \left(\frac{\sqrt{2}\pi\hbar c}{\sqrt{3}\sigma_2}\right)^3 \left(1 + \frac{m_1}{m_3} + \frac{m_2}{m_3}\right)^3 \gamma \delta(\mathbf{p}_1 + \mathbf{p}_2 - \frac{m_1+m_2}{m_3} \mathbf{p}_3) \delta(\sum_{i=1}^2 \mathbf{p}_i - \mathbf{p}) \\ &= 8^2 N_{h_1 h_2 h_3} g_{H_j} \gamma^2 \left(\frac{\hbar^2 c^2 \pi}{\sqrt{3}\sigma_1 \sigma_2}\right)^3 \int d\mathbf{x}_1 d\mathbf{x}_2 d\mathbf{x}_3 f_{h_1 h_2 h_3}^{(n)}(\mathbf{x}_1, \mathbf{x}_2, \mathbf{x}_3; \frac{m_1 \mathbf{p}}{m_1+m_2+m_3}, \frac{m_2 \mathbf{p}}{m_1+m_2+m_3}, \frac{m_3 \mathbf{p}}{m_1+m_2+m_3}) \\ &\times e^{-\frac{(\mathbf{x}'_1 - \mathbf{x}'_2)^2}{2\sigma_1^2}} e^{-\frac{2(\frac{m_1 \mathbf{x}'_1}{m_1+m_2} + \frac{m_2 \mathbf{x}'_2}{m_1+m_2} - \mathbf{x}'_3)^2}{3\sigma_2^2}}. \end{aligned} \quad (20)$$

Changing coordinate variables in Eq. (20) to be $\mathbf{Y} = (m_1 \mathbf{x}_1 + m_2 \mathbf{x}_2 + m_3 \mathbf{x}_3)/(m_1 + m_2 + m_3)$, $\mathbf{r}_1 = (\mathbf{x}_1 - \mathbf{x}_2)/\sqrt{2}$ and $\mathbf{r}_2 = \sqrt{\frac{2}{3}}(\frac{m_1 \mathbf{x}_1}{m_1+m_2} + \frac{m_2 \mathbf{x}_2}{m_1+m_2} - \mathbf{x}_3)$, we have

$$f_{H_j}(\mathbf{p}) = 8^2 N_{h_1 h_2 h_3} g_{H_j} \gamma^2 \left(\frac{\hbar^2 c^2 \pi}{\sqrt{3}\sigma_1 \sigma_2}\right)^3 3^{3/2} \int d\mathbf{Y} d\mathbf{r}_1 d\mathbf{r}_2 f_{h_1 h_2 h_3}^{(n)}(\mathbf{Y}, \mathbf{r}_1, \mathbf{r}_2; \frac{m_1 \mathbf{p}}{m_1+m_2+m_3}, \frac{m_2 \mathbf{p}}{m_1+m_2+m_3}, \frac{m_3 \mathbf{p}}{m_1+m_2+m_3}) e^{-\frac{r_1^2}{\sigma_1^2}} e^{-\frac{r_2^2}{\sigma_2^2}}. \quad (21)$$

We also assume the center of mass coordinate in joint distribution is factorized, i.e.,

$$\begin{aligned} &3^{3/2} f_{h_1 h_2 h_3}^{(n)}(\mathbf{Y}, \mathbf{r}_1, \mathbf{r}_2; \frac{m_1 \mathbf{p}}{m_1+m_2+m_3}, \frac{m_2 \mathbf{p}}{m_1+m_2+m_3}, \frac{m_3 \mathbf{p}}{m_1+m_2+m_3}) \\ &= f_{h_1 h_2 h_3}^{(n)}(\mathbf{Y}) f_{h_1 h_2 h_3}^{(n)}(\mathbf{r}_1, \mathbf{r}_2; \frac{m_1 \mathbf{p}}{m_1+m_2+m_3}, \frac{m_2 \mathbf{p}}{m_1+m_2+m_3}, \frac{m_3 \mathbf{p}}{m_1+m_2+m_3}). \end{aligned} \quad (22)$$

Substituting Eq. (22) into Eq. (21), we have

$$f_{H_j}(\mathbf{p}) = 8^2 N_{h_1 h_2 h_3} g_{H_j} \gamma^2 \left(\frac{\hbar^2 c^2 \pi}{\sqrt{3}\sigma_1 \sigma_2}\right)^3 \int d\mathbf{r}_1 d\mathbf{r}_2 f_{h_1 h_2 h_3}^{(n)}(\mathbf{r}_1, \mathbf{r}_2; \frac{m_1 \mathbf{p}}{m_1+m_2+m_3}, \frac{m_2 \mathbf{p}}{m_1+m_2+m_3}, \frac{m_3 \mathbf{p}}{m_1+m_2+m_3}) e^{-\frac{r_1^2}{\sigma_1^2}} e^{-\frac{r_2^2}{\sigma_2^2}}. \quad (23)$$

Adopting gaussian forms for the relative coordinate distributions [49, 54], we have

$$\begin{aligned} &f_{h_1 h_2 h_3}^{(n)}(\mathbf{r}_1, \mathbf{r}_2; \frac{m_1 \mathbf{p}}{m_1+m_2+m_3}, \frac{m_2 \mathbf{p}}{m_1+m_2+m_3}, \frac{m_3 \mathbf{p}}{m_1+m_2+m_3}) \\ &= \frac{1}{[\pi C_1 R_f^2(\mathbf{p})]^{3/2}} e^{-\frac{r_1^2}{C_1 R_f^2(\mathbf{p})}} \frac{1}{[\pi C_2 R_f^2(\mathbf{p})]^{3/2}} e^{-\frac{r_2^2}{C_2 R_f^2(\mathbf{p})}} f_{h_1 h_2 h_3}^{(n)}(\frac{m_1 \mathbf{p}}{m_1+m_2+m_3}, \frac{m_2 \mathbf{p}}{m_1+m_2+m_3}, \frac{m_3 \mathbf{p}}{m_1+m_2+m_3}). \end{aligned} \quad (24)$$

Comparing relations of \mathbf{r}_1 , \mathbf{r}_2 with \mathbf{x}_1 , \mathbf{x}_2 , \mathbf{x}_3 to that of \mathbf{r} with \mathbf{x}_1 , \mathbf{x}_2 in Sec. II A, we see that C_1 is equal to C_w and C_2 is $4C_w/3$ when ignoring the mass difference of m_1 and m_2 [49, 54]. Substituting Eq. (24) into Eq. (23) and considering the Lorentz transformation, we integrate from the relative coordinate variables and obtain

$$\begin{aligned} f_{H_j}(\mathbf{p}) &= \frac{64\pi^3 \hbar^6 c^6 g_{H_j} \gamma^2}{3\sqrt{3} [C_1 R_f^2(\mathbf{p}) + \sigma_1^2] \sqrt{C_1 [R_f(\mathbf{p})/\gamma]^2 + \sigma_1^2} [C_2 R_f^2(\mathbf{p}) + \sigma_2^2] \sqrt{C_2 [R_f(\mathbf{p})/\gamma]^2 + \sigma_2^2}} \\ &\times f_{h_1 h_2 h_3}(\frac{m_1 \mathbf{p}}{m_1+m_2+m_3}, \frac{m_2 \mathbf{p}}{m_1+m_2+m_3}, \frac{m_3 \mathbf{p}}{m_1+m_2+m_3}). \end{aligned} \quad (25)$$

Ignoring correlations between h_1 , h_2 and h_3 , we have the three-dimensional momentum distribution of H_j as

$$f_{H_j}(\mathbf{p}) = \frac{64\pi^3 \hbar^6 c^6 g_{H_j} \gamma^2}{3 \sqrt{3} [C_1 R_f^2(\mathbf{p}) + \sigma_1^2] \sqrt{C_1 [R_f(\mathbf{p})/\gamma]^2 + \sigma_1^2} [C_2 R_f^2(\mathbf{p}) + \sigma_2^2] \sqrt{C_2 [R_f(\mathbf{p})/\gamma]^2 + \sigma_2^2}} \times f_{h_1}\left(\frac{m_1 \mathbf{p}}{m_1 + m_2 + m_3}\right) f_{h_2}\left(\frac{m_2 \mathbf{p}}{m_1 + m_2 + m_3}\right) f_{h_3}\left(\frac{m_3 \mathbf{p}}{m_1 + m_2 + m_3}\right). \quad (26)$$

Finally we have the Lorentz invariant momentum distribution as

$$f_{H_j}^{(inv)}(p_T, y) = \frac{64\pi^3 \hbar^6 c^6 g_{H_j}}{3 \sqrt{3} [C_1 R_f^2(p_T, y) + \sigma_1^2] \sqrt{C_1 [R_f(p_T, y)/\gamma]^2 + \sigma_1^2} [C_2 R_f^2(p_T, y) + \sigma_2^2] \sqrt{C_2 [R_f(p_T, y)/\gamma]^2 + \sigma_2^2}} \frac{m_{H_j}}{m_1 m_2 m_3} \times f_{h_1}^{(inv)}\left(\frac{m_1 p_T}{m_1 + m_2 + m_3}, y\right) f_{h_2}^{(inv)}\left(\frac{m_2 p_T}{m_1 + m_2 + m_3}, y\right) f_{h_3}^{(inv)}\left(\frac{m_3 p_T}{m_1 + m_2 + m_3}, y\right). \quad (27)$$

As a short summary of this section, we want to state that Eqs. (15) and (27) give the relationships of dibaryon states and tribaryon states with primordial baryons in momentum space in the laboratory frame. They clearly show effects of different factors on dibaryon or tribaryon production such as the whole hadronic system scale as well as the sizes of the formed composite objects. They can be directly used to calculate the p_T distributions, the rapidity distributions and even the total yields of light (hyper-)nuclei as long as the primordial baryon momentum distributions are given. Formulas for the antiparticles are the same as these dibaryon and tribaryon states, and we leave out the duplication. Their applications at midrapidity (i.e., $y = 0$) in heavy ion collisions at the LHC will be shown in the following sections.

III. RESULTS OF LIGHT NUCLEI

In this section, we use the coalescence model to study productions of d , ${}^3\text{He}$ and t at midrapidity in Pb+Pb collisions at $\sqrt{s_{NN}} = 5.02$ TeV. We first calculate the coalescence factors B_2 , B_3 and discuss their centrality and p_T -dependent behaviors. We then compute the p_T spectra of d , ${}^3\text{He}$ and t . We finally calculate the averaged transverse momenta $\langle p_T \rangle$, the yield rapidity densities dN/dy and yield ratios of different light nuclei.

A. The coalescence factor of light nuclei

The coalescence factor B_A is defined as

$$B_A(p_T) = f_{d, {}^3\text{He}, t}^{(inv)}(p_T) / \left\{ \left[f_p^{(inv)}\left(\frac{p_T}{A}\right) \right]^Z \left[f_n^{(inv)}\left(\frac{p_T}{A}\right) \right]^{A-Z} \right\}, \quad (28)$$

where A is the mass number and Z is the charge of the light nuclei. From Eqs. (15) and (27), we respectively have for d ,

${}^3\text{He}$ and t

$$B_2(p_T) = \frac{m_d g_d (\sqrt{2\pi} \hbar c)^3}{m_p m_n [C_w R_f^2(p_T) + \sigma_d^2] \sqrt{C_w [R_f(p_T)/\gamma]^2 + \sigma_d^2}}, \quad (29)$$

$$B_3(p_T) = \frac{64\pi^3 \hbar^6 c^6 g_{{}^3\text{He}}}{3 \sqrt{3} [C_1 R_f^2(p_T) + \sigma_{{}^3\text{He}}^2] \sqrt{C_1 [R_f(p_T)/\gamma]^2 + \sigma_{{}^3\text{He}}^2}} \times \frac{m_{{}^3\text{He}}}{m_p^2 m_n [C_2 R_f^2(p_T) + \sigma_{{}^3\text{He}}^2] \sqrt{C_2 [R_f(p_T)/\gamma]^2 + \sigma_{{}^3\text{He}}^2}}, \quad (30)$$

$$B_3(p_T) = \frac{64\pi^3 \hbar^6 c^6 g_t}{3 \sqrt{3} [C_1 R_f^2(p_T) + \sigma_t^2] \sqrt{C_1 [R_f(p_T)/\gamma]^2 + \sigma_t^2}} \times \frac{m_t}{m_p m_n^2 [C_2 R_f^2(p_T) + \sigma_t^2] \sqrt{C_2 [R_f(p_T)/\gamma]^2 + \sigma_t^2}}. \quad (31)$$

Here $\sigma_d = \sqrt{\frac{4}{3}} R_d$, and the root-mean-square radius of the deuteron $R_d = 2.1421$ fm [57]. $\sigma_{{}^3\text{He}} = R_{{}^3\text{He}} = 1.9661$ fm and $\sigma_t = R_t = 1.7591$ fm [57]. $m_{p,n}$ denotes the nucleon mass and $m_{d, {}^3\text{He}, t}$ the mass of the d , ${}^3\text{He}$ and t . Eqs. (29-31) show that p_T -dependent behaviors of B_2 and B_3 are related with the Lorentz contraction factor γ and $R_f(p_T)$.

To further compute B_2 and B_3 , the specific form of $R_f(p_T)$ is necessary. Similar as in Ref. [50], the dependence of $R_f(p_T)$ on centrality and p_T is considered to factorize into a linear dependence on the cube root of the pseudorapidity density of charged particles $(dN_{ch}/d\eta)^{1/3}$ and a power-law dependence on the transverse mass of the formed light nucleus m_T [59]. So we have

$$R_f(p_T) = a \times (dN_{ch}/d\eta)^{1/3} \times \left(\sqrt{p_T^2 + m_{d, {}^3\text{He}, t}^2} \right)^b, \quad (32)$$

where a and b are free parameters. Their values in Pb+Pb collisions at $\sqrt{s_{NN}} = 5.02$ TeV are (0.70, -0.31) for d and (0.66, -0.31) for ${}^3\text{He}$ and t , which are determined by reproducing the data of the p_T spectra of d and ${}^3\text{He}$ in the most central 0-5% centrality. Here b is set to be centrality independent, which is consistent with that in hydrodynamics [60] and

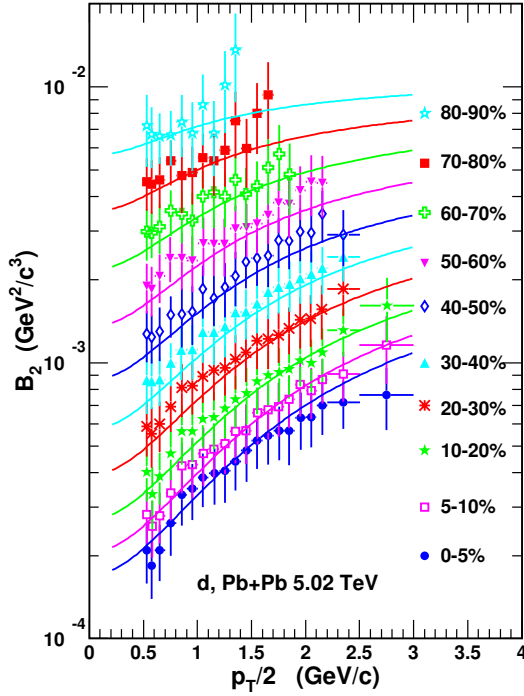


FIG. 1. The B_2 of d as a function of $p_T/2$ in different centralities in Pb+Pb collisions at $\sqrt{s_{NN}} = 5.02$ TeV. Symbols with error bars are experimental data [58] and solid lines are theoretical results.

that in STAR measurements of two-pion interferometry in central and simicentral Au+Au collisions [61]. Note that $b < 0$ gives decreasing R_f with the increasing p_T . This means that nucleons with stronger collective motions have larger probability to emit from the same spatial location. Such coordinate-momentum correlation is naturally given by the gaussian form of the relative coordinate distribution in Eqs. (11) and (24). a is also set to be centrality-independent, the same as that in our previous work [50].

We use the data of $dN_{ch}/d\eta$ in Ref. [62] to evaluate R_f , and then compute coalescence factors B_2 and B_3 . Fig. 1 shows B_2 of d as a function of the transverse momentum scaled by the mass number $p_T/2$ in different centralities in Pb+Pb collisions at $\sqrt{s_{NN}} = 5.02$ TeV. Symbols with error bars are experimental data [58] and solid lines are theoretical results of the coalescence model. From Fig. 1, one can see from central to peripheral collisions, B_2 exhibits an increasing trend, which is due to the decreasing size of the created hadronic system. For the same centrality, B_2 increase as a function of $p_T/2$. This increase behavior results on one hand from the Lorentz contraction factor γ , which has been studied in Ref. [49]. On the other hand, it results from the decreasing R_f with increasing p_T . The rising behavior of the experimental data as a function of $p_T/2$ from central to peripheral collisions can be quantitatively described by the coalescence model.

Fig. 2 shows B_3 of ${}^3\text{He}$ and that of \bar{t} as a function of $p_T/3$ in different centralities in Pb+Pb collisions at $\sqrt{s_{NN}} = 5.02$ TeV. Symbols with error bars are experimental data [22] and solid lines are theoretical results. Similarly as B_2 , experimen-

tal data of B_3 also exhibits a rising trend as a function of $p_T/3$, which is reproduced well by the coalescence model from central to peripheral collisions. Fig. 1 and Fig. 2 show that the centrality and momentum dependent behaviors of B_2 and B_3 in Pb+Pb collisions at $\sqrt{s_{NN}} = 5.02$ TeV are simultaneously explained by the coalescence model. The influencing factors of B_2 and B_3 are explicitly unfolded, as shown in Eqs. (29–31). Some other models based on transport approach are also used to study behaviors of B_A in heavy ion collisions at the high LHC energies [63–66]. All the results from these different models can help cross understand production properties of light nuclei from different aspects.

B. The p_T spectra of light nuclei

The p_T spectra of primordial nucleons are necessary inputs for computing p_T distributions of light nuclei in the coalescence model. We here use the blast-wave model to get p_T distribution functions of primordial protons by fitting the experimental data of prompt (anti)protons in Ref. [62]. The blast-wave function [67] is given as

$$\frac{d^2N}{2\pi p_T dp_T dy} \propto \int_0^R r dr m_T I_0 \left(\frac{p_T \sinh \rho}{T_{kin}} \right) K_1 \left(\frac{m_T \cosh \rho}{T_{kin}} \right), \quad (33)$$

where r is the radial distance in the transverse plane and R is the radius of the fireball. I_0 and K_1 are the modified Bessel functions, and the velocity profile $\rho = \tanh^{-1}[\beta_s (\frac{r}{R})^n]$. The surface velocity β_s , the kinetic freeze-out temperature T_{kin} and n are fitting parameters.

Fig. 3 shows the p_T spectra of prompt protons plus antiprotons in different centralities in Pb+Pb collisions at $\sqrt{s_{NN}} = 5.02$ TeV. Symbols with error bars are experimental data [62], and dashed lines are the results of the blast-wave model. The p_T spectra in different centralities are scaled by different factors for clarity as shown in the figure. For the primordial neutron p_T spectra, we adopt the same as those of primordial protons as we focus on light nucleus production at midrapidity at so high LHC energy that the isospin symmetry is well satisfied.

We first calculate the p_T spectra of deuterons in Pb+Pb collisions at $\sqrt{s_{NN}} = 5.02$ TeV in 0–5%, 5–10%, 10–20%, 20–30%, 30–40%, 40–50%, 50–60%, 60–70%, 70–80% and 80–90% centralities. Different solid lines scaled by different factors for clarity in Fig. 4 are our theoretical results. Symbols with error bars are experimental data from the ALICE collaboration [22]. We then compute the p_T spectra of ${}^3\text{He}$ and \bar{t} in Pb+Pb collisions at $\sqrt{s_{NN}} = 5.02$ TeV in different centralities. Different solid lines in Fig. 5 are our theoretical results, which agree with the available data denoted by filled symbols [22]. From Fig. 4 and Fig. 5, one can see the nucleon coalescence is still the dominant mechanism for light nuclei production in Pb+Pb collisions at $\sqrt{s_{NN}} = 5.02$ TeV. More precise measurements for ${}^3\text{He}$ and \bar{t} in wide p_T range in the forthcoming future can help further test the coalescence mechanism, especially in peripheral Pb+Pb collisions.

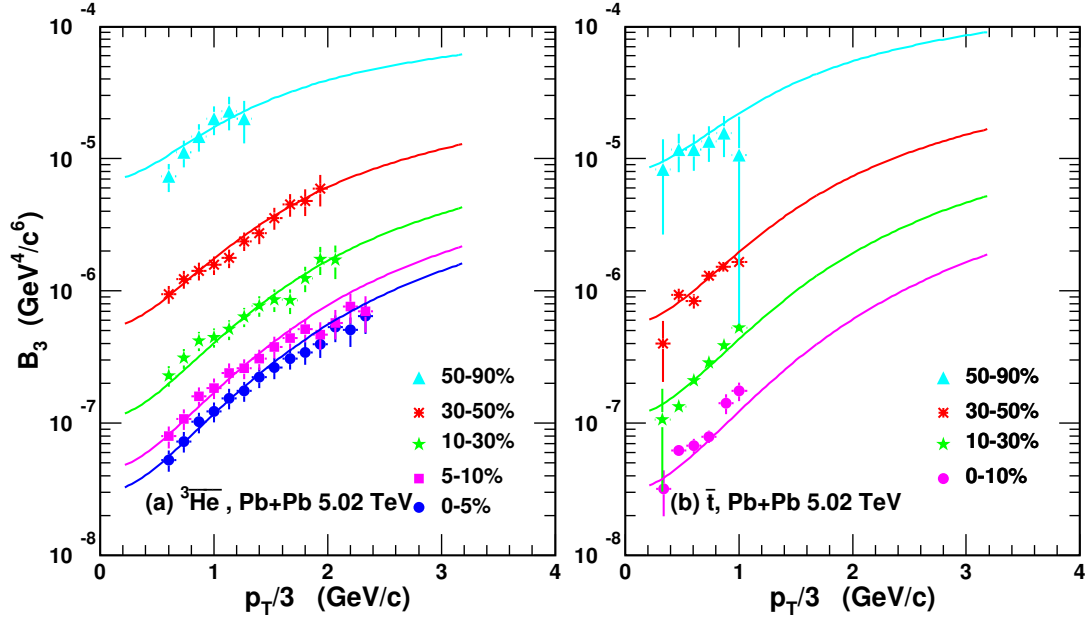


FIG. 2. The B_3 of (a) ${}^3\overline{\text{He}}$ and (b) \bar{i} as a function of $p_T/3$ in different centralities in Pb+Pb collisions at $\sqrt{s_{NN}} = 5.02$ TeV. Symbols with error bars are experimental data [22] and solid lines are theoretical results.

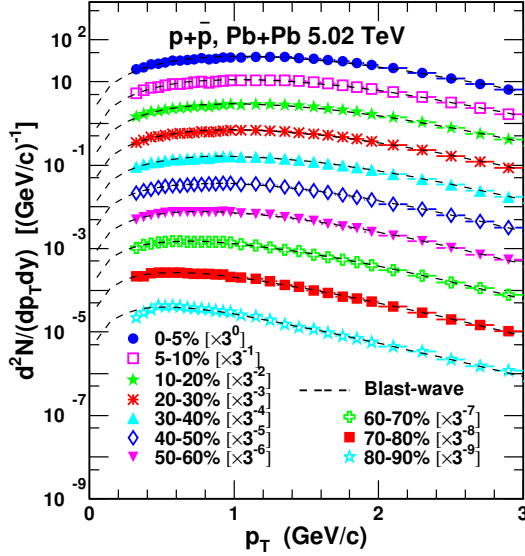


FIG. 3. The p_T spectra of prompt protons plus antiprotons in different centralities in Pb+Pb collisions at $\sqrt{s_{NN}} = 5.02$ TeV. Symbols with error bars are experimental data [62], and dashed lines are results of the blast-wave model.

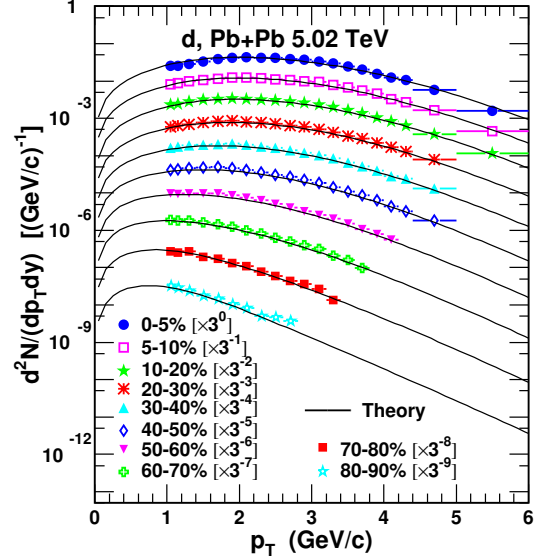


FIG. 4. The p_T spectra of deuterons in different centralities in Pb+Pb collisions at $\sqrt{s_{NN}} = 5.02$ TeV. Symbols with error bars are experimental data [58] and solid lines are theoretical results.

C. Averaged transverse momenta and yield rapidity densities of light nuclei

We here study the averaged transverse momenta $\langle p_T \rangle$ and yield rapidity densities dN/dy of d , ${}^3\overline{\text{He}}$ and \bar{i} . Our theoretical results are put in the fourth and sixth columns in Table I. Experimental data in the third and fifth columns are from Refs. [22, 58]. A clear decreasing trend for both $\langle p_T \rangle$ and

dN/dy from central to peripheral collisions is observed. This is due to that in more central collisions more energy is deposited in the midrapidity region and collective evolution exists longer. Theoretical results for d , ${}^3\overline{\text{He}}$ and \bar{i} are consistent with the corresponding data within the experimental uncertainties except a very little underestimation for the dN/dy of \bar{i} in peripheral 50-90% collision. Such underestimation needs to be confirmed by future precise data.

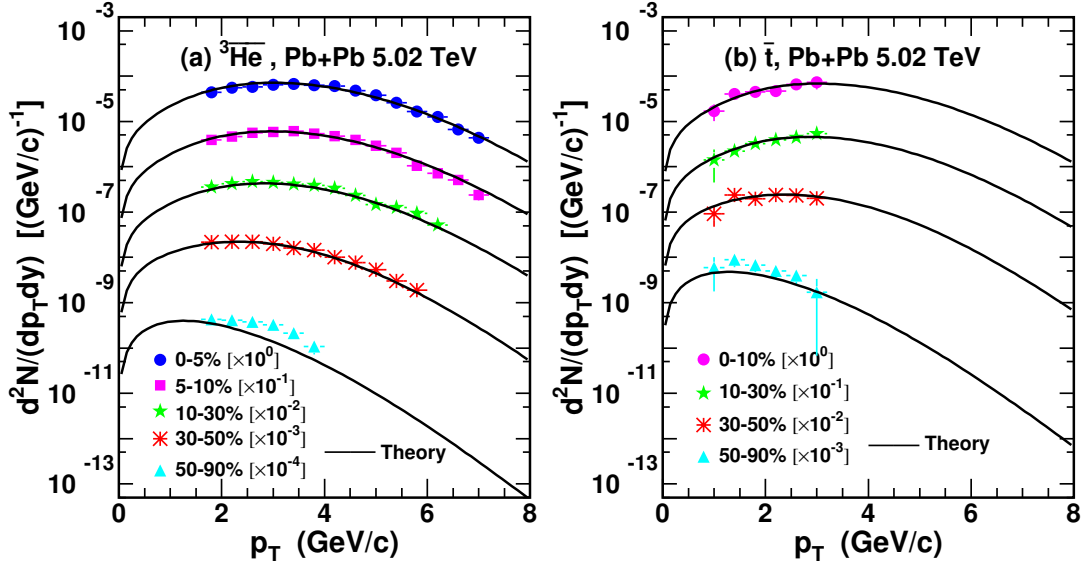


FIG. 5. The p_T spectra of (a) ${}^3\text{He}$ and (b) \bar{t} in different centralities in Pb+Pb collisions at $\sqrt{s_{NN}} = 5.02$ TeV. Filled symbols with error bars are experimental data [22] and solid lines are theoretical results.

TABLE I. Averaged transverse momenta $\langle p_T \rangle$ and yield rapidity densities dN/dy of d , ${}^3\text{He}$ and \bar{t} in different centralities in Pb+Pb collisions at $\sqrt{s_{NN}} = 5.02$ TeV. Experimental data in the third and fifth columns are from Refs. [22, 58]. Theoretical results are in the fourth and sixth columns.

	Centrality	$\langle p_T \rangle$ (GeV)		dN/dy	
		Data	Theory	Data	Theory
d	0-5%	$2.45 \pm 0.00 \pm 0.09$	2.37	$(1.19 \pm 0.00 \pm 0.21) \times 10^{-1}$	1.22×10^{-1}
	5-10%	$2.41 \pm 0.01 \pm 0.10$	2.33	$(1.04 \pm 0.00 \pm 0.19) \times 10^{-1}$	1.01×10^{-1}
	10-20%	$2.34 \pm 0.00 \pm 0.11$	2.28	$(8.42 \pm 0.02 \pm 1.50) \times 10^{-2}$	7.86×10^{-2}
	20-30%	$2.21 \pm 0.00 \pm 0.12$	2.18	$(6.16 \pm 0.02 \pm 1.10) \times 10^{-2}$	5.58×10^{-2}
	30-40%	$2.05 \pm 0.00 \pm 0.12$	2.04	$(4.25 \pm 0.01 \pm 0.75) \times 10^{-2}$	3.82×10^{-2}
	40-50%	$1.88 \pm 0.01 \pm 0.12$	1.87	$(2.73 \pm 0.01 \pm 0.48) \times 10^{-2}$	2.46×10^{-2}
	50-60%	$1.70 \pm 0.01 \pm 0.11$	1.66	$(1.62 \pm 0.01 \pm 0.28) \times 10^{-2}$	1.47×10^{-2}
	60-70%	$1.46 \pm 0.01 \pm 0.12$	1.45	$(8.35 \pm 0.14 \pm 1.43) \times 10^{-3}$	7.58×10^{-3}
	70-80%	$1.27 \pm 0.02 \pm 0.11$	1.25	$(3.52 \pm 0.06 \pm 0.63) \times 10^{-3}$	3.22×10^{-3}
${}^3\text{He}$	80-90%	$1.09 \pm 0.02 \pm 0.40$	1.10	$(1.13 \pm 0.03 \pm 0.23) \times 10^{-3}$	0.925×10^{-3}
	0-5%	$3.465 \pm 0.013 \pm 0.154 \pm 0.144$	3.26	$(24.70 \pm 0.28 \pm 2.29 \pm 0.30) \times 10^{-5}$	25.6×10^{-5}
	5-10%	$3.368 \pm 0.014 \pm 0.141 \pm 0.132$	3.21	$(20.87 \pm 0.26 \pm 1.95 \pm 0.43) \times 10^{-5}$	21.4×10^{-5}
	10-30%	$3.237 \pm 0.021 \pm 0.157 \pm 0.150$	3.08	$(15.94 \pm 0.31 \pm 1.53 \pm 0.34) \times 10^{-5}$	14.8×10^{-5}
	30-50%	$2.658 \pm 0.016 \pm 0.084 \pm 0.049$	2.64	$(7.56 \pm 0.13 \pm 0.70 \pm 0.10) \times 10^{-5}$	7.16×10^{-5}
\bar{t}	50-90%	$2.057 \pm 0.023 \pm 0.090 \pm 0.027$	1.77	$(1.19 \pm 0.08 \pm 0.16 \pm 0.14) \times 10^{-5}$	0.931×10^{-5}
	0-10%	$3.368 \pm 0.241 \pm 0.060$	3.27	$(24.45 \pm 1.75 \pm 2.71) \times 10^{-5}$	24.6×10^{-5}
	10-30%	$3.015 \pm 0.286 \pm 0.040$	3.11	$(14.19 \pm 1.35 \pm 1.29) \times 10^{-5}$	15.9×10^{-5}
	30-50%	$2.524 \pm 0.593 \pm 0.180$	2.68	$(7.24 \pm 1.70 \pm 0.65) \times 10^{-5}$	7.97×10^{-5}
	50-90%	$1.636 \pm 0.226 \pm 0.040$	1.80	$(1.66 \pm 0.23 \pm 0.16) \times 10^{-5}$	1.14×10^{-5}

D. Yield ratios of light nuclei

Yield ratios of light nuclei carry information of intrinsic production correlations of different light nuclei and are predicted to have nontrivial behaviors [50]. In this subsection we study centrality dependence of different yield ratios, such as

$$d/p, {}^3\text{He}/\bar{p}, d/p^2, {}^3\text{He}/\bar{p}^3 \text{ and } \bar{t}/{}^3\text{He}.$$

Fig. 6 (a) and (b) show the $dN_{ch}/d\eta$ dependence of d/p and ${}^3\text{He}/\bar{p}$ in Pb+Pb collisions at $\sqrt{s_{NN}} = 5.02$ TeV. Filled circles with error bars are experimental data [68], and open circles connected with dashed lines to guide the eye are theoretical results. From Eq. (15) we approximately have the p_T -integrated

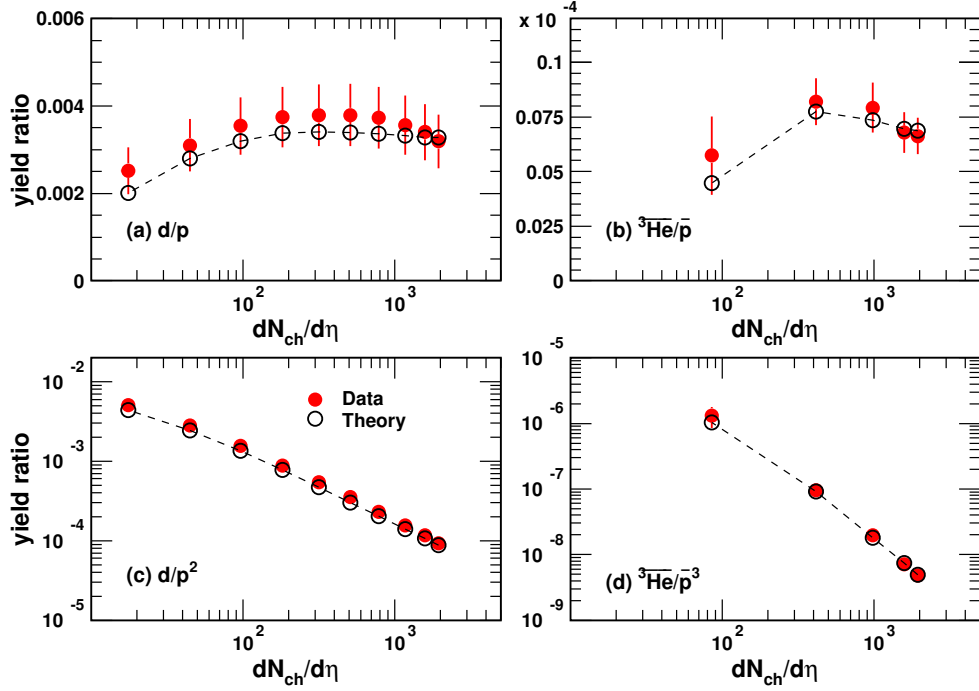


FIG. 6. Yield ratios (a) d/p , (b) ${}^3\text{He}/\bar{p}$, (c) d/p^2 and (d) ${}^3\text{He}/\bar{p}^3$ as a function of $dN_{ch}/d\eta$ in Pb+Pb collisions at $\sqrt{s_{NN}} = 5.02$ TeV. Filled circles with error bars are experimental data [22, 58] and open circles connected with dashed lines to guide the eye are theoretical results.

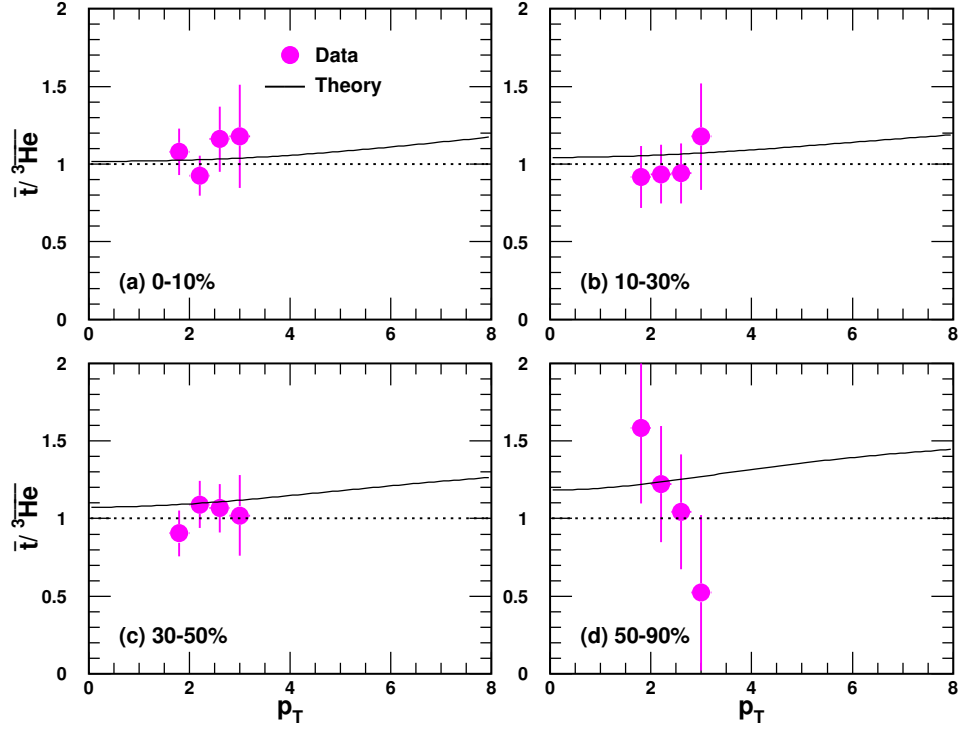


FIG. 7. Yield ratio $\bar{t}/{}^3\text{He}$ as a function of p_T in different centralities in Pb+Pb collisions at $\sqrt{s_{NN}} = 5.02$ TeV. Filled circles with error bars are experimental data [22] and solid lines are theoretical results.

yield ratio

$$\frac{d}{p} \propto \frac{N_p}{\langle R_f \rangle^3 \left(C_w + \frac{\sigma_d^2}{\langle R_f \rangle^2} \right) \sqrt{\frac{C_w}{\langle \gamma \rangle^2} + \frac{\sigma_d^2}{\langle R_f \rangle^2}}}$$

$$= \frac{N_p}{\langle R_f \rangle^3 / \langle \gamma \rangle} \times \frac{1}{\left(C_w + \frac{\sigma_d^2}{\langle R_f \rangle^2} \right) \sqrt{C_w + \frac{\sigma_d^2}{\langle R_f \rangle^2 / \langle \gamma \rangle^2}}}, \quad (34)$$

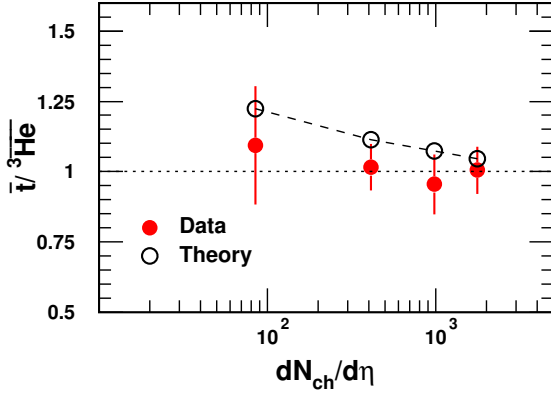


FIG. 8. Yield ratio $\bar{t}/^3\text{He}$ as a function of $dN_{ch}/d\eta$ in Pb+Pb collisions at $\sqrt{s_{NN}} = 5.02$ TeV. Filled circles with error bars are experimental data [22] and open circles connected with dashed lines to guide the eye are theoretical results.

where angle brackets denote the averaged values. Eq. (34) gives that the $dN_{ch}/d\eta$ -dependent behavior of d/p is determined by two factors. One is the nucleon number density $\frac{N_p}{\langle R_f^3 \rangle \langle \gamma \rangle}$ and the other is the suppression effect from the relative size of the formed light nuclei to the hadronic source system $\frac{\sigma_d}{\langle R_f \rangle}$. Similar case holds for $^3\text{He}/\bar{p}$. The nucleon number density decreases especially from semicentral to central collisions [62], which makes d/p and $^3\text{He}/\bar{p}$ decrease with the increasing $dN_{ch}/d\eta$. The relative size $\frac{\sigma_d}{\langle R_f \rangle}$ decreases and its suppression effect becomes weak in large hadronic systems, which makes d/p and $^3\text{He}/\bar{p}$ increase with the increasing $dN_{ch}/d\eta$ [69]. For very high $dN_{ch}/d\eta$ area, difference of the suppression extents in different centralities becomes insignificant and the decreasing nucleon number density dominates the decreasing behavior of d/p and $^3\text{He}/\bar{p}$. For low $dN_{ch}/d\eta$ area, different suppression extents of the relative size in different centralities make d/p and $^3\text{He}/\bar{p}$ increase as a function of $dN_{ch}/d\eta$. The finally conjunct result from the nucleon number density and the suppression effect makes d/p and $^3\text{He}/\bar{p}$ first increase from peripheral to semicentral collisions and then decrease from semicentral to central collisions, just as shown from semicentral to central collisions of Fig. 6 (a) and (b).

Fig. 6 (c) and (d) show d/p^2 and $^3\text{He}/\bar{p}^3$ as a function of $dN_{ch}/d\eta$ in Pb+Pb collisions at $\sqrt{s_{NN}} = 5.02$ TeV. Filled circles with error bars are experimental data [68]. Open circles connected with dashed lines to guide the eye are the theoretical results. Both of them give explicit decreasing trend with the increasing $dN_{ch}/d\eta$, which are very different from the previous d/p and $^3\text{He}/\bar{p}$. Recalling that d/p^2 and $^3\text{He}/\bar{p}^3$ represent the probability of any pn -pair coalescing into a deuteron and that of any $\bar{p}\bar{p}\bar{n}$ -cluster coalescing into a ^3He . This means that it is more difficult for any pn -pair or $\bar{p}\bar{p}\bar{n}$ -cluster to recombine into a deuteron or ^3He in larger hadronic system produced in more central collisions.

The yield ratio $\bar{t}/^3\text{He}$ is proposed to be a valuable probe to distinguish the thermal production and the coalescence production for light nuclei [50]. In the coalescence picture, it

is always larger than one and approaches to one at large R_f where the suppression effect from the nucleus size can be ignored. The smaller R_f , the higher deviation of $\bar{t}/^3\text{He}$ from one. The same case holds for $\bar{t}/^3\text{He}$. Fig. 7 shows $\bar{t}/^3\text{He}$ as a function of p_T in Pb+Pb collisions at $\sqrt{s_{NN}} = 5.02$ TeV in different centralities 0-10%, 10-30%, 30-50% and 50-90%. Filled circles with error bars are experimental data [22] and solid lines are the theoretical results. Reference line of one is plotted with dotted lines. With the increasing p_T , R_f decreases, so our theoretical results increase. This feature is very different from that in the thermal model, where the expectation for this ratio is one [33]. The trend of the data in 0-10%, 10-30% and 30-50% centralities indicates an increasing hint but a final conclusion is hard to make due to the limited p_T range and the large error bars. Data in the peripheral 50-90% centrality seems decrease, but further more precise measurements are needed to confirm. More precise data in near future can be used to further distinguish production mechanisms of ^3He and \bar{t} .

The p_T -integrated yield ratio $\bar{t}/^3\text{He}$ as a function of $dN_{ch}/d\eta$ is in Fig. 8. Filled circles with error bars are experimental data [22] and open circles connected with the dashed line to guide the eye are theoretical results. Reference line of one is also plotted with the dotted line. $\bar{t}/^3\text{He}$ exhibits a decreasing trend. This is because larger $dN_{ch}/d\eta$, i.e., larger R_f , makes $\bar{t}/^3\text{He}$ decrease closer to one. Theoretical results of $\bar{t}/^3\text{He}$ in the coalescence model give non-flat behaviors as a function of $dN_{ch}/d\eta$. This is due to different relative production suppression between ^3He and \bar{t} at different hadronic system scales.

IV. RESULTS OF THE HYPERTRITON AND Ω -HYPERNUCLEI

In this section, we use the coalescence model in Sec. II to study productions of the hypertriton and Ω -hypernuclei. We give the results of the p_T spectra, the averaged p_T and yield rapidity densities of the $^3_\Lambda\text{H}$. We present the predictions of different Ω -hypernuclei, such as $H(p\Omega^-)$, $H(n\Omega^-)$ and $H(pn\Omega^-)$. We propose two groups of observables, both of which exhibit novel behaviors. One group of observables are the averaged p_T ratios of the light (hyper-)nuclei to the protons (hyperons), and the other are centrality-dependent yield ratios of theirs.

A. The p_T spectra of Λ and Ω^- hyperons

The p_T spectra of Λ and Ω^- hyperons are necessary for computing p_T distributions of $^3_\Lambda\text{H}$ and Ω -hypernuclei. We use the blast-wave model to get p_T distribution functions by fitting the experimental data of Λ and Ω^- in Pb+Pb collisions at $\sqrt{s_{NN}} = 5.02$ TeV [70]. They are shown in Fig. 9. Filled symbols with error bars are experimental data [70], and dashed lines are the results of the blast-wave model. The p_T spectra in 0-10%, 10-30% and 30-50% centralities are scaled by 2^0 , 2^{-1} and 2^{-2} , respectively, for clarity in the figure. We have also studied the p_T spectra of Λ and Ω^- hyperons with

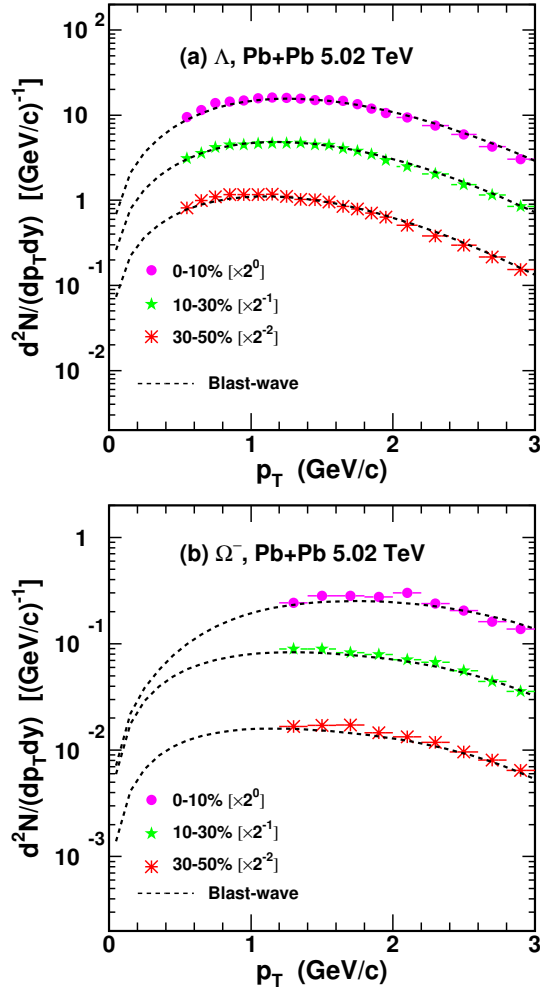


FIG. 9. The p_T spectra of (a) Λ and (b) Ω^- in Pb+Pb collisions at $\sqrt{s_{NN}} = 5.02$ TeV. Symbols with error bars are experimental data [70] and dashed lines are results of the blast-wave model.

the Quark Combination Model developed by the Shandong group (SDQCM) in another work [71], where the results are consistent with the blast-wave model at low and intermediate p_T regions. We in the following use these Λ and Ω^- hyperons in Fig. 9 to compute the productions of the ${}^3_\Lambda\text{H}$ and Ω^- hypernuclei. The values of parameters a and b in $R_f(p_T)$ for $H(p\Omega^-)$ and $H(n\Omega^-)$ are the same with that of the deuteron, and those for ${}^3_\Lambda\text{H}$ and $H(pn\Omega^-)$ are the same with ${}^3\text{He}$. So our calculated results for the ${}^3_\Lambda\text{H}$ and Ω^- hypernuclei are parameter-free, and they are more potent for further test of the coalescence mechanism in describing the productions of nuclei with strangeness flavor quantum number.

B. The results of the ${}^3_\Lambda\text{H}$

Based on Eq. (27), we in this subsection compute the production of the ${}^3_\Lambda\text{H}$. Considering that the experimental measurements of the ${}^3_\Lambda\text{H}$ suggest a halo structure with a d core

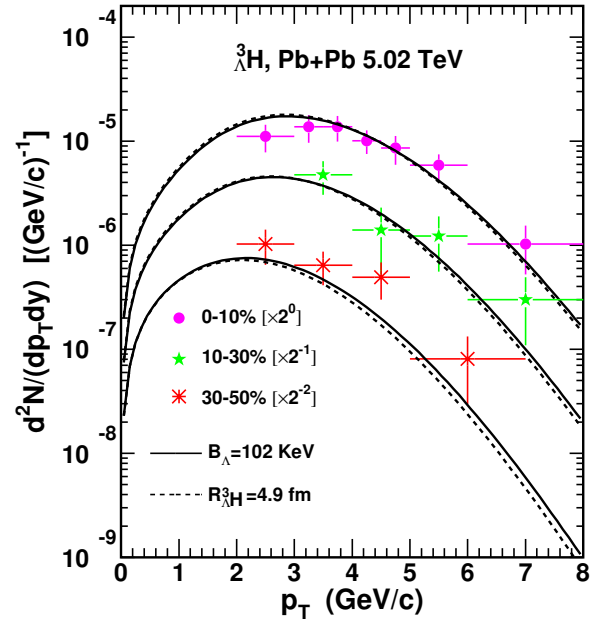


FIG. 10. The p_T spectra of the ${}^3_\Lambda\text{H}$ in Pb+Pb collisions at $\sqrt{s_{NN}} = 5.02$ TeV. Filled symbols with error bars are the experimental data [51]. The solid and dashed lines are the theoretical results with a halo structure and a spherical shape, respectively.

encircled by a Λ , we first use $\sigma_1 = \sqrt{\frac{2(m_p+m_n)^2}{3(m_p^2+m_n^2)}}R_d$ fm and $\sigma_2 = \sqrt{\frac{2(m_d+m_\Lambda)^2}{9(m_d^2+m_\Lambda^2)}}r_{\Lambda d}$. The $\Lambda - d$ distance $r_{\Lambda d}$ is evaluated via $r_{\Lambda d} = \sqrt{\hbar^2/(4\mu B_\Lambda)}$ [72], where μ is the reduced mass and the binding energy B_Λ here is adopted to be the latest and most precise measurement to date 102 KeV [25]. We also take a spherical shape for the ${}^3_\Lambda\text{H}$ to execute the calculation to study the influence of the shape on its production. In this case, $\sigma_1 = \sqrt{\frac{m_\Lambda(m_p+m_n)(m_p+m_n+m_\Lambda)}{m_p m_n(m_p+m_n)+m_n m_\Lambda(m_n+m_\Lambda)+m_\Lambda m_p(m_\Lambda+m_p)}}R_{\Lambda}^3\text{H}$, and $\sigma_2 = \sqrt{\frac{4m_p m_n(m_p+m_n+m_\Lambda)^2}{3(m_p+m_n)[m_p m_n(m_p+m_n)+m_n m_\Lambda(m_n+m_\Lambda)+m_\Lambda m_p(m_\Lambda+m_p)]}}R_{\Lambda}^3\text{H}$, where the root-mean-square radius $R_{\Lambda}^3\text{H}$ is adopted to be 4.9 fm [11]. Fig. 10 shows the p_T spectra of the ${}^3_\Lambda\text{H}$ in 0-10%, 10-30% and 30-50% centralities in Pb+Pb collisions at $\sqrt{s_{NN}} = 5.02$ TeV. Filled symbols with error bars are the experimental data [51]. The solid lines are the theoretical results of the coalescence model with a halo structure and the dashed lines are those for a spherical shape. The p_T spectra in different centralities are scaled by different factors for clarity as shown in the figure. From Fig. 10, one can see that there exists a weak difference in the theoretical results of the p_T spectra between a halo structure and a spherical shape, and the latter gives a little softer p_T spectra. The results with a halo structure approach to the available data better, both for amplitude and for shape. This point can also be seen in the results of the averaged transverse momenta $\langle p_T \rangle$ and yield rapidity densities dN/dy of ${}^3_\Lambda\text{H}$ hereunder.

Table II presents the averaged transverse momenta $\langle p_T \rangle$ and yield rapidity densities dN/dy of ${}^3_\Lambda\text{H}$ in different centralities in

TABLE II. Averaged transverse momenta $\langle p_T \rangle$ and yield rapidity densities dN/dy of ${}^3_\Lambda\text{H}$ in different centralities in Pb+Pb collisions at $\sqrt{s_{NN}} = 5.02$ TeV. Experimental data in the seventh column are from Ref. [51]. Theory-4.9 denotes theoretical results with a spherical shape at $R_{\Lambda\text{H}} = 4.9$ fm. Theory-102, Theory-148 and Theory-410 denote theoretical results with a halo structure at $B_\Lambda = 102, 148$ and 410 KeV, respectively.

Centrality		$\langle p_T \rangle$ (GeV)				dN/dy ($\times 10^{-5}$)				
		Theory-4.9	Theory-102	Theory-148	Theory-410	Data	Theory-4.9	Theory-102	Theory-148	Theory-410
$^3_\Lambda\text{H}$	0-10%	3.16	3.19	3.24	3.37	$4.83 \pm 0.23 \pm 0.57$	6.09	5.96	7.75	12.7
	10-30%	2.90	2.94	2.99	3.11	$2.62 \pm 0.25 \pm 0.40$	2.98	2.99	4.07	7.44
	30-50%	2.46	2.52	2.55	2.65	$1.27 \pm 0.10 \pm 0.14$	0.875	0.932	1.35	2.94

Pb+Pb collisions at $\sqrt{s_{NN}} = 5.02$ TeV. Experimental data in the seventh column are from Ref. [51]. Theory-4.9 in the third and eighth columns denotes theoretical results with a spherical shape at $R_{\Lambda\text{H}} = 4.9$ fm. Theory-102 in the fourth and ninth columns are theoretical results at $B_\Lambda = 102$ KeV. Theory-148 in the fifth and tenth columns are theoretical results at a word averaged value of $B_\Lambda = 148$ KeV [25]. We also give theoretical results at $B_\Lambda = 410$ KeV measured by the STAR collaboration [23] in the sixth and eleventh columns. A clear decreasing trend for both $\langle p_T \rangle$ and dN/dy from central to semi-central collisions is observed. This is the same as light nuclei, which is due to that in more central collisions more energy is deposited in the midrapidity region and collective evolution exists longer. For the halo structure, with the increase of the B_Λ , the size of the ${}^3_\Lambda\text{H}$ decreases, and the suppression effect from the ${}^3_\Lambda\text{H}$ size becomes relatively weak. This leads to an increase for dN/dy with the increasing B_Λ . Besides dN/dy , such production suppression effect also affects the p_T distribution [50, 73]. This is because the suppression effect becomes stronger with larger nucleus size in smaller system. Recalling that $R_f(p_T)$ decreases with p_T , the ${}^3_\Lambda\text{H}$ production is more suppressed in larger p_T areas in the case of larger ${}^3_\Lambda\text{H}$ size. So there exists a decreasing trend for $\langle p_T \rangle$ with the decreasing B_Λ , as shown in Table II. This is the reason why the $\langle p_T \rangle$ of ${}^3_\Lambda\text{H}$ is even smaller than that of the triton while the $\langle p_T \rangle$ of Λ is larger than the nucleon.

C. Predictions of Ω -hypernuclei

The nucleon- Ω dibaryon in the S-wave and spin-2 channel is an interesting candidate of the deuteron-like state [74]. The HAL QCD collaboration has reported the root mean square radius of $H(p\Omega^-)$ is about 3.24 fm and that of $H(n\Omega^-)$ is 3.77 fm [75]. According to Eq. (15), we study the productions of $H(p\Omega^-)$ and $H(n\Omega^-)$, where the spin degeneracy factor $g_{H(p\Omega^-)} = g_{H(n\Omega^-)} = 5/8$. Fig. 11 shows predictions for their p_T spectra in 0-10%, 10-30% and 30-50% centralities with solid, dashed and dash-dotted lines, respectively, in Pb+Pb collisions at $\sqrt{s_{NN}} = 5.02$ TeV. Different lines are scaled by different factors for clarity as shown in the figure.

Table III presents predictions of the averaged transverse momenta $\langle p_T \rangle$ and yield rapidity densities dN/dy of $H(p\Omega^-)$ and $H(n\Omega^-)$. Both of them decrease from central to semi-central collisions, similar as light nuclei and the ${}^3_\Lambda\text{H}$. The very

TABLE III. Predictions of averaged transverse momenta $\langle p_T \rangle$ and yield rapidity densities dN/dy of $H(p\Omega^-)$ and $H(n\Omega^-)$ in different centralities in Pb+Pb collisions at $\sqrt{s_{NN}} = 5.02$ TeV.

	Centrality	$\langle p_T \rangle$ (GeV)	dN/dy ($\times 10^{-4}$)
$H(p\Omega^-)$	0-10%	2.84	9.80
	10-30%	2.44	6.27
	30-50%	2.18	2.16
$H(n\Omega^-)$	0-10%	2.81	8.75
	10-30%	2.41	5.46
	30-50%	2.15	1.79

slight low results of $H(n\Omega^-)$ than $H(p\Omega^-)$ come from its slightly larger size. Our predictions for dN/dy of $H(p\Omega^-)$ and $H(n\Omega^-)$ are in the same magnitude with BLWC and AMPTC models in Ref. [76].

The $H(pn\Omega^-)$ with maximal spin- $\frac{5}{2}$ is proposed to be one of the most promising partners of the t and ${}^3_\Lambda\text{H}$ with multi-strangeness flavor quantum number [77]. With Eq. (27), we study its production, and the spin degeneracy factor $g_{H(pn\Omega^-)} = 3/8$. As its root-mean-square radius $R_{H(pn\Omega^-)}$ is undetermined, we adopt 1.5, 2.0 and 2.5 fm to execute calculations, respectively. Fig. 12 shows predictions of the p_T spectra in 0-10%, 10-30% and 30-50% centralities in Pb+Pb collisions at $\sqrt{s_{NN}} = 5.02$ TeV. Solid, dashed and dash-dotted lines denote results with $R_{H(pn\Omega^-)} = 1.5, 2.0$ and 2.5 fm, respectively, which are scaled by different factors for clarity as shown in the figure.

Table IV presents predictions of the averaged transverse momenta $\langle p_T \rangle$ and yield rapidity densities dN/dy of $H(pn\Omega^-)$ in different centralities in Pb+Pb collisions at $\sqrt{s_{NN}} = 5.02$ TeV. Theory-1.5, Theory-2.0 and Theory-2.5 denote theoretical results at $R_{H(pn\Omega^-)} = 1.5, 2.0$ and 2.5 fm, respectively. Our predictions for dN/dy are in the same magnitude with those in Ref. [78].

D. Averaged transverse momentum ratios and yield ratios

Based on the results of light nuclei and hypernuclei above, we find two groups of interesting observables which are powerful probes for the nucleus production mechanism. One group of observables are the $\langle p_T \rangle$ ratios of light nuclei to protons and hypernuclei to hyperons. The other are the centrality-

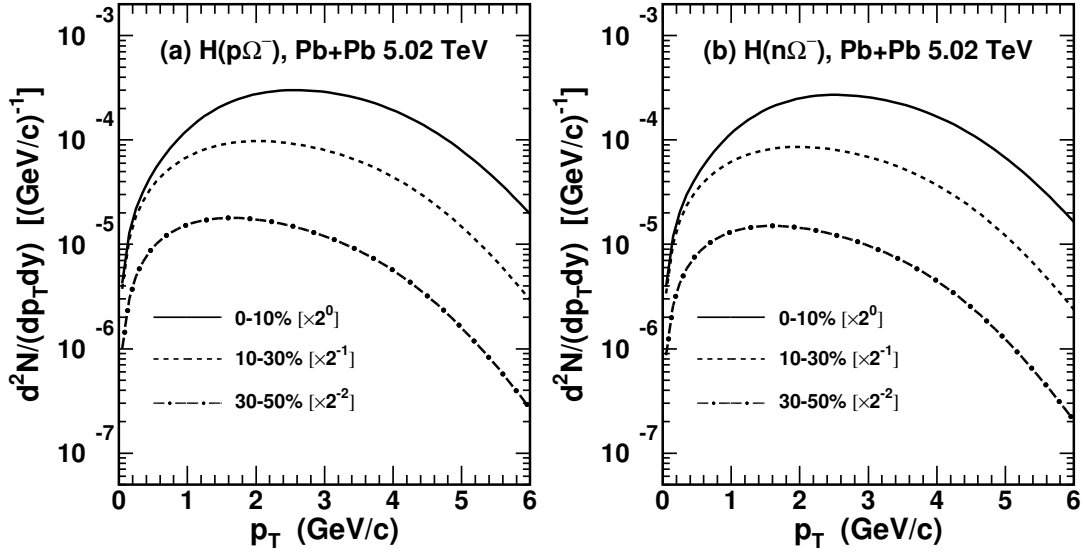


FIG. 11. Predictions of the p_T spectra of (a) $H(p\Omega^-)$ and (b) $H(n\Omega^-)$ in different centralities in Pb+Pb collisions at $\sqrt{s_{NN}} = 5.02$ TeV.

TABLE IV. Predictions of averaged transverse momenta $\langle p_T \rangle$ and yield rapidity densities dN/dy of $H(pn\Omega^-)$ in different centralities in Pb+Pb collisions at $\sqrt{s_{NN}} = 5.02$ TeV. Theory-1.5, Theory-2.0 and Theory-2.5 denote theoretical results at $R_{H(pn\Omega^-)} = 1.5, 2.0$ and 2.5 fm, respectively.

Centrality	$\langle p_T \rangle$ (GeV)			dN/dy ($\times 10^{-6}$)		
	Theory-1.5	Theory-2.0	Theory-2.5	Theory-1.5	Theory-2.0	Theory-2.5
0-10%	3.94	3.88	3.82	4.77	4.17	3.56
10-30%	3.44	3.36	3.29	3.50	2.95	2.41
30-50%	2.98	2.89	2.81	1.60	1.24	0.92

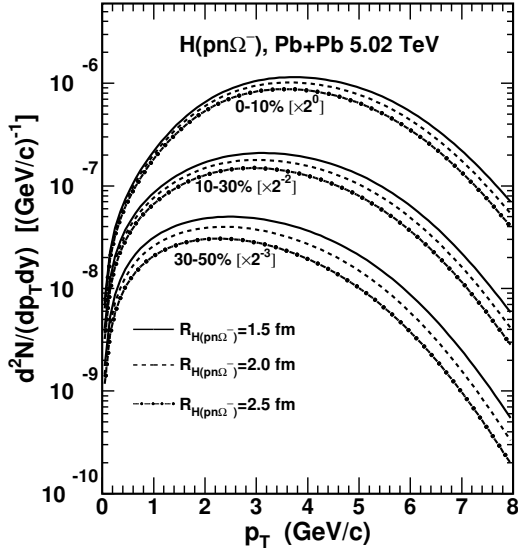


FIG. 12. Predictions of the p_T spectra of $H(pn\Omega^-)$ in different centralities in Pb+Pb collisions at $\sqrt{s_{NN}} = 5.02$ TeV.

dependent yield ratios of theirs.

Fig. 13 (a) and (b) show the $\langle p_T \rangle$ ratios of dibaryon states

to baryons and those of tribaryon states to baryons, i.e., $\frac{\langle p_T \rangle_d}{\langle p_T \rangle_p}$, $\frac{\langle p_T \rangle_{H(p\Omega^-)}}{\langle p_T \rangle_{\Omega^-}}$, $\frac{\langle p_T \rangle_{H(n\Omega^-)}}{\langle p_T \rangle_{\Omega^-}}$, $\frac{\langle p_T \rangle_t}{\langle p_T \rangle_p}$, $\frac{\langle p_T \rangle_{^3\text{He}}}{\langle p_T \rangle_p}$, $\frac{\langle p_T \rangle_{^3\text{H}}}{\langle p_T \rangle_{\Lambda}}$ and $\frac{\langle p_T \rangle_{H(pn\Omega^-)}}{\langle p_T \rangle_{\Omega^-}}$. Open symbols connected by dashed lines to guide the eyes are the theoretical results of the coalescence model. All these $\langle p_T \rangle$ ratios increase as a function of $dN_{ch}/d\eta$ due to the stronger collective flow in more central collisions. More interestingly, these $\langle p_T \rangle$ ratios of light nuclei to protons and hypernuclei to hyperons happen to offset the $\langle p_T \rangle$ differences of p , Λ and Ω^- . This makes them more powerful to bring characteristics resulted from the production mechanism to light. Both dibaryon-to-baryon and tribaryon-to-baryon $\langle p_T \rangle$ ratios exhibit a distinct reverse-hierarchy of the light (hyper-)nucleus sizes at any centrality, i.e., $\frac{\langle p_T \rangle_d}{\langle p_T \rangle_p} > \frac{\langle p_T \rangle_{H(p\Omega^-)}}{\langle p_T \rangle_{\Omega^-}} > \frac{\langle p_T \rangle_{H(n\Omega^-)}}{\langle p_T \rangle_{\Omega^-}}$ as $R_d < R_{H(p\Omega^-)} < R_{H(n\Omega^-)}$, and $\frac{\langle p_T \rangle_t}{\langle p_T \rangle_p} > \frac{\langle p_T \rangle_{^3\text{He}}}{\langle p_T \rangle_p} > \frac{\langle p_T \rangle_{H(pn\Omega^-)}}{\langle p_T \rangle_{\Omega^-}} > \frac{\langle p_T \rangle_{^3\text{H}}}{\langle p_T \rangle_{\Lambda}}$ as $R_t < R_{^3\text{He}} < R_{H(pn\Omega^-)} < R_{^3\text{H}}$. Here we take $R_{H(pn\Omega^-)} = 2$ fm. Such reverse-hierarchy comes from stronger production suppression for light (hyper-) nuclei with larger sizes in higher p_T region. This production property is very different from the thermal model in which these ratios are approximately equal to each other [33].

Fig. 13 (c) and (d) show yield ratios of dibaryon states to baryons and those of tribaryon states to baryons. Open symbols connected with dashed lines to guide the eye are the the-

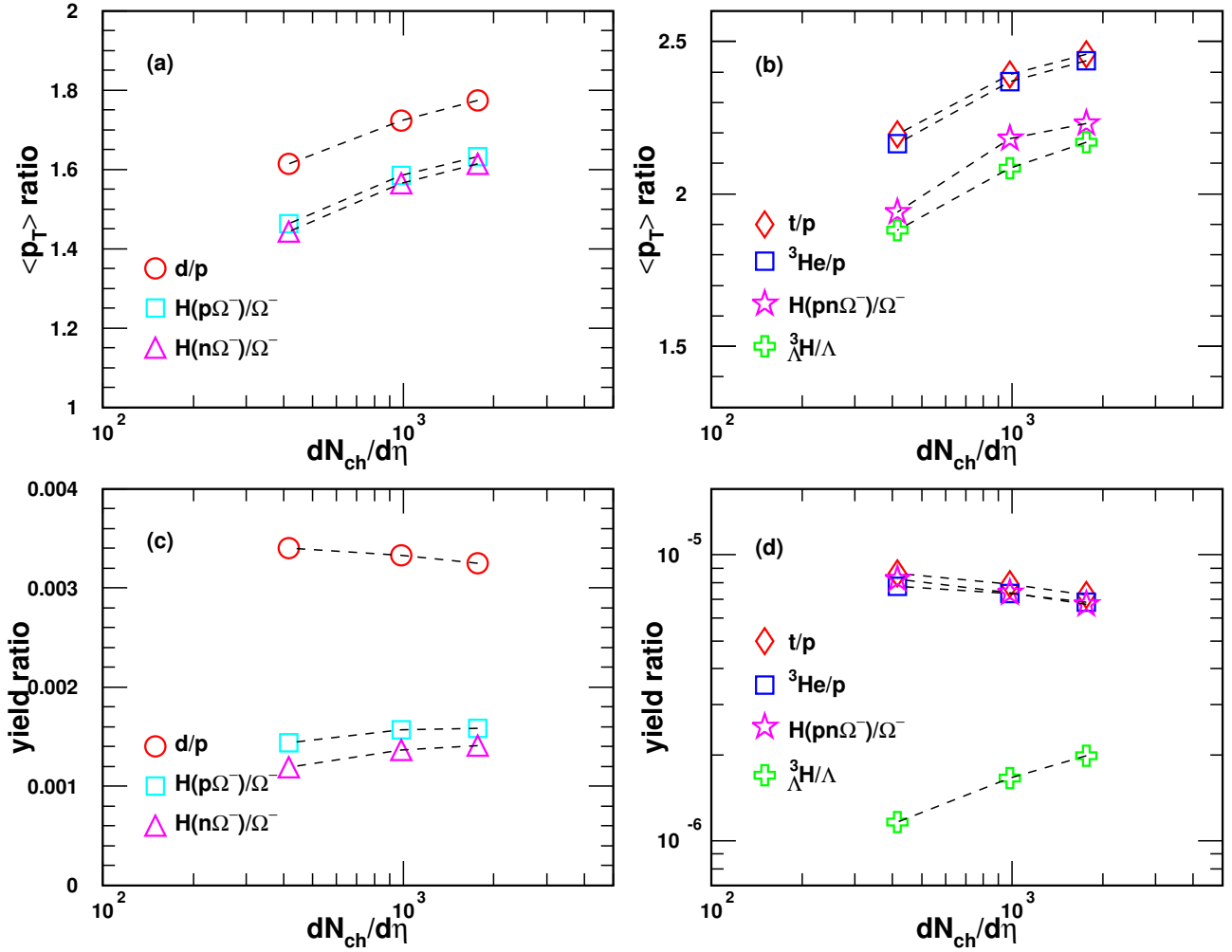


FIG. 13. The $\langle p_T \rangle$ ratios of (a) dibaryon states to baryons, (b) tribaryon states to baryons and the yield ratios of (c) dibaryon states to baryons, (d) tribaryon states to baryons as a function of $dN_{ch}/d\eta$ in Pb+Pb collisions at $\sqrt{s_{NN}} = 5.02$ TeV.

oretical results of the coalescence model. Some of these ratios such as d/p , t/p , ${}^3\text{He}/p$ and $H(pn\Omega^-)/\Omega^-$ decrease while the others $H(p\Omega^-)/\Omega^-$, $H(n\Omega^-)/\Omega^-$ and ${}^3\text{H}/\Lambda$ increase as a function of $dN_{ch}/d\eta$. From Eqs. (15) and (27), similar as Eq. (34), we approximately have

$$\begin{aligned} \frac{d}{p} &\sim \frac{H(p\Omega^-)}{\Omega^-} \sim \frac{H(n\Omega^-)}{\Omega^-} \\ &\propto \frac{N_p}{\langle R_f \rangle^3 \left(C_w + \frac{\sigma_{d,H(p\Omega^-),H(n\Omega^-)}}{\langle R_f \rangle^2} \right) \sqrt{\frac{C_w}{\langle \gamma \rangle^2} + \frac{\sigma_{d,H(p\Omega^-),H(n\Omega^-)}}{\langle R_f \rangle^2}}} \\ &= \frac{N_p}{\langle R_f \rangle^3 \langle \gamma \rangle} \times \frac{1}{\left(C_w + \frac{\sigma_{d,H(p\Omega^-),H(n\Omega^-)}}{\langle R_f \rangle^2} \right) \sqrt{C_w + \frac{\sigma_{d,H(p\Omega^-),H(n\Omega^-)}}{\langle R_f \rangle^2 \langle \gamma \rangle^2}}} \end{aligned} \quad (35)$$

and

$$\frac{t}{p} \sim \frac{{}^3\text{He}}{p} \sim \frac{{}^3\text{H}}{\Lambda} \sim \frac{H(pn\Omega^-)}{\Omega^-}$$

$$\begin{aligned} &\propto \frac{N_p^2}{\langle R_f \rangle^6 \left(C_w + \frac{\sigma_1^2}{\langle R_f \rangle^2} \right) \sqrt{\frac{C_w}{\langle \gamma \rangle^2} + \frac{\sigma_1^2}{\langle R_f \rangle^2}}} \\ &\times \frac{1}{\left(\frac{4C_w}{3} + \frac{\sigma_2^2}{\langle R_f \rangle^2} \right) \sqrt{\frac{4C_w}{3\langle \gamma \rangle^2} + \frac{\sigma_2^2}{\langle R_f \rangle^2}}} \\ &= \left(\frac{N_p}{\langle R_f \rangle^3 \langle \gamma \rangle} \right)^2 \frac{1}{\left(C_w + \frac{\sigma_1^2}{\langle R_f \rangle^2} \right) \sqrt{C_w + \frac{\sigma_1^2}{\langle R_f \rangle^2 \langle \gamma \rangle^2}}} \\ &\times \frac{1}{\left(\frac{4C_w}{3} + \frac{\sigma_2^2}{\langle R_f \rangle^2} \right) \sqrt{\frac{4C_w}{3} + \frac{\sigma_2^2}{\langle R_f \rangle^2 \langle \gamma \rangle^2}}}. \end{aligned} \quad (36)$$

Eqs. (35) and (36) show that centrality-dependent behaviors of these two-particle yield ratios closely relate with the nucleon number density $\frac{N_p}{\langle R_f \rangle^3 \langle \gamma \rangle}$ and the production suppression effect via the relative size of nuclei to hadronic source systems

$\frac{\sigma_i}{\langle R_f \rangle}$ ($i = d, H(p\Omega^-), H(n\Omega^-), 1, 2$ and $\sigma_i \propto$ the corresponding nucleus size).

For the limit case of the nuclei with very small (negligible) sizes compared to the hadronic system scale, the $dN_{ch}/d\eta$ -dependent behaviors of their yield ratios to baryons are completely determined by the nucleon number density. For the general case, the item $\frac{\sigma_i}{\langle R_f \rangle}$ suppresses these ratios and such suppression becomes weaker in larger hadronic systems. This makes these yield ratios increase from peripheral to central collisions, i.e., with the increasing $dN_{ch}/d\eta$. The larger nucleus size, the stronger increase as a function of $dN_{ch}/d\eta$. The nucleon density decreases with increasing $dN_{ch}/d\eta$ [62], which makes these ratios decrease. As the root-mean-square radii of d , t , ${}^3\text{He}$ and $H(pn\Omega^-)$ are about or smaller than 2 fm, the decreasing nucleon density dominates the behaviors of their yield ratios to baryons. But for $H(p\Omega^-)$, $H(n\Omega^-)$ and ${}^3\text{H}$, their root-mean-square radii are larger than 3 fm, the production suppression effect from their sizes becomes dominant, which leads their yield ratios to baryons increase as a function of $dN_{ch}/d\eta$. Such different centrality-dependent behaviors can help to justify the nucleus own sizes in future experiments for more light nuclei and hypernuclei.

V. SUMMARY

We extended the analytical coalescence model previously developed for the productions of light nuclei to include the hyperon coalescence to study production characteristics of d , ${}^3\text{He}$, \bar{t} , ${}^3\text{H}$ and Ω -hypernuclei. We derived the formula of the momentum distribution of two baryons coalescing into dibaryon states and that of three baryons coalescing into tribaryon states. The relationships of dibaryon states and tribaryon states with primordial baryons in momentum space in the laboratory frame were given. The effects of the hadronic

system scale and the nucleus own size on the nucleus production were also clearly presented.

We applied the extended coalescence model to Pb+Pb collisions at $\sqrt{s_{NN}} = 5.02$ TeV. We explained the available data of the B_2 and B_3 , the p_T spectra, averaged transverse momenta and yield rapidity densities of the d , ${}^3\text{He}$, \bar{t} , and ${}^3\text{H}$ measured by the ALICE collaboration. We provided predictions of the p_T spectra, averaged transverse momenta and yield rapidity densities of different Ω -hypernuclei, e.g., $H(p\Omega^-)$, $H(n\Omega^-)$, and $H(pn\Omega^-)$, for future experimental measurements.

More interestingly, we found two groups of novel observables. One group referred to the averaged transverse momentum ratio $\frac{\langle p_T \rangle_d}{\langle p_T \rangle_p}$, $\frac{\langle p_T \rangle_{H(p\Omega^-)}}{\langle p_T \rangle_{\Omega^-}}$, $\frac{\langle p_T \rangle_{H(n\Omega^-)}}{\langle p_T \rangle_{\Omega^-}}$, $\frac{\langle p_T \rangle_{\bar{t}}}{\langle p_T \rangle_p}$, $\frac{\langle p_T \rangle_{{}^3\text{He}}}{\langle p_T \rangle_p}$, $\frac{\langle p_T \rangle_{{}^3\text{H}}}{\langle p_T \rangle_{\Lambda}}$, $\frac{\langle p_T \rangle_{H(pn\Omega^-)}}{\langle p_T \rangle_{\Omega^-}}$. They exhibited a reverse-hierarchy according to the sizes of the nuclei themselves at any collision centrality. The other group involved the centrality-dependent yield ratios d/p , $H(p\Omega^-)/\Omega^-$, $H(n\Omega^-)/\Omega^-$, t/p , ${}^3\text{He}/p$, ${}^3\text{H}/\Lambda$ and $H(pn\Omega^-)/\Omega^-$. Some of these yield ratios d/p , t/p , ${}^3\text{He}/p$ and $H(pn\Omega^-)/\Omega^-$ decreased while the others $H(p\Omega^-)/\Omega^-$, $H(n\Omega^-)/\Omega^-$ and ${}^3\text{H}/\Lambda$ increased as a function of $dN_{ch}/d\eta$ in the same coalescence framework. Such different trends were caused by different production suppression degrees from the nucleus size. The behaviors of these two groups of ratios in the coalescence mechanism were different from the thermal model. They were powerful probes of the nucleus production mechanism and can help judge the nucleus own sizes.

ACKNOWLEDGEMENTS

This work was supported in part by the National Natural Science Foundation of China under Grants No. 12175115 and No. 12375074.

-
- [1] J. Chen, D. Keane, Y.-G. Ma, A. Tang, and Z. Xu, *Phys. Rept.* **760**, 1 (2018), [arXiv:1808.09619 \[nucl-ex\]](#).
 - [2] H. H. Gutbrod, A. Sandoval, P. J. Johansen, A. M. Poskanzer, J. Gosset, W. G. Meyer, G. D. Westfall, and R. Stock, *Phys. Rev. Lett.* **37**, 667 (1976).
 - [3] J. Aichelin, *Phys. Rept.* **202**, 233 (1991).
 - [4] A. Andronic, P. Braun-Munzinger, K. Redlich, and J. Stachel, *Nature* **561**, 321 (2018), [arXiv:1710.09425 \[nucl-th\]](#).
 - [5] A. Bzdak, S. Esumi, V. Koch, J. Liao, M. Stephanov, and N. Xu, *Phys. Rept.* **853**, 1 (2020), [arXiv:1906.00936 \[nucl-th\]](#).
 - [6] K.-J. Sun, L.-W. Chen, C. M. Ko, and Z. Xu, *Phys. Lett. B* **774**, 103 (2017), [arXiv:1702.07620 \[nucl-th\]](#).
 - [7] K.-J. Sun, L.-W. Chen, C. M. Ko, J. Pu, and Z. Xu, *Phys. Lett. B* **781**, 499 (2018), [arXiv:1801.09382 \[nucl-th\]](#).
 - [8] X. Luo, S. Shi, N. Xu, and Y. Zhang, *Particles* **3**, 278 (2020), [arXiv:2004.00789 \[nucl-ex\]](#).
 - [9] J. Steinheimer, M. Mitrovski, T. Schuster, H. Petersen, M. Bleicher, and H. Stoecker, *Phys. Lett. B* **676**, 126 (2009), [arXiv:0811.4077 \[hep-ph\]](#).
 - [10] S. R. Beane, E. Chang, S. D. Cohen, W. Detmold, H. W. Lin, T. C. Luu, K. Orginos, A. Parreno, M. J. Savage, and A. Walker-Loud (NPLQCD), *Phys. Rev. D* **87**, 034506 (2013), [arXiv:1206.5219 \[hep-lat\]](#).
 - [11] H. Nemura, Y. Suzuki, Y. Fujiwara, and C. Nakamoto, *Prog. Theor. Phys.* **103**, 929 (2000), [arXiv:nucl-th/9912065](#).
 - [12] P. Jannnarkar and N. Mathur, *Phys. Rev. Lett.* **123**, 162003 (2019), [arXiv:1906.06054 \[hep-lat\]](#).
 - [13] K. Morita, S. Gongyo, T. Hatsuda, T. Hyodo, Y. Kamiya, and A. Ohnishi, *Phys. Rev. C* **101**, 015201 (2020), [arXiv:1908.05414 \[nucl-th\]](#).
 - [14] S. Afnasiev et al. (PHENIX), *Phys. Rev. Lett.* **99**, 052301 (2007), [arXiv:nucl-ex/0703024](#).
 - [15] T. Anticic et al. (NA49), *Phys. Rev. C* **94**, 044906 (2016), [arXiv:1606.04234 \[nucl-ex\]](#).
 - [16] C. Adler et al. (STAR), *Phys. Rev. Lett.* **87**, 262301 (2001), [Erratum: *Phys. Rev. Lett.* **87**, 279902 (2001)], [arXiv:nucl-ex/0108022](#).

- [17] L. Adamczyk *et al.* (STAR), *Phys. Rev. C* **94**, 034908 (2016), [arXiv:1601.07052 \[nucl-ex\]](#).
- [18] J. Adam *et al.* (STAR), *Phys. Rev. C* **102**, 044906 (2020), [arXiv:2007.04609 \[nucl-ex\]](#).
- [19] J. Adam *et al.* (STAR), *Phys. Rev. C* **99**, 064905 (2019), [arXiv:1903.11778 \[nucl-ex\]](#).
- [20] M. Abdulhamid *et al.* (STAR), *Phys. Rev. Lett.* **130**, 202301 (2023), [arXiv:2209.08058 \[nucl-ex\]](#).
- [21] S. Acharya *et al.* (ALICE), *Phys. Rev. C* **102**, 055203 (2020), [arXiv:2005.14639 \[nucl-ex\]](#).
- [22] S. Acharya *et al.* (ALICE), *Phys. Rev. C* **107**, 064904 (2023), [arXiv:2211.14015 \[nucl-ex\]](#).
- [23] J. Adam *et al.* (STAR), *Nature Phys.* **16**, 409 (2020), [arXiv:1904.10520 \[hep-ex\]](#).
- [24] M. Abdallah *et al.* (STAR), *Phys. Rev. Lett.* **128**, 202301 (2022), [arXiv:2110.09513 \[nucl-ex\]](#).
- [25] S. Acharya *et al.* (ALICE), *Phys. Rev. Lett.* **131**, 102302 (2023), [arXiv:2209.07360 \[nucl-ex\]](#).
- [26] J. Adam *et al.* (ALICE), *Phys. Lett. B* **754**, 360 (2016), [arXiv:1506.08453 \[nucl-ex\]](#).
- [27] P. Braun-Munzinger and B. Dönigus, *Nucl. Phys. A* **987**, 144 (2019), [arXiv:1809.04681 \[nucl-ex\]](#).
- [28] D. Oliinychenko, *Nucl. Phys. A* **1005**, 121754 (2021), [arXiv:2003.05476 \[hep-ph\]](#).
- [29] S. Mrowczynski, *Eur. Phys. J. ST* **229**, 3559 (2020), [arXiv:2004.07029 \[nucl-th\]](#).
- [30] B. Dönigus, G. Röpke, and D. Blaschke, *Phys. Rev. C* **106**, 044908 (2022), [arXiv:2206.10376 \[nucl-th\]](#).
- [31] C. B. Dover, U. W. Heinz, E. Schnedermann, and J. Zimanyi, *Phys. Rev. C* **44**, 1636 (1991).
- [32] L.-W. Chen, C. M. Ko, and B.-A. Li, *Phys. Rev. C* **68**, 017601 (2003), [arXiv:nucl-th/0302068](#).
- [33] A. Andronic, P. Braun-Munzinger, J. Stachel, and H. Stöcker, *Phys. Lett. B* **697**, 203 (2011), [arXiv:1010.2995 \[nucl-th\]](#).
- [34] A. Mekjian, *Phys. Rev. Lett.* **38**, 640 (1977).
- [35] P. J. Siemens and J. I. Kapusta, *Phys. Rev. Lett.* **43**, 1486 (1979).
- [36] J. Cleymans, S. Kabana, I. Kraus, H. Oeschler, K. Redlich, and N. Sharma, *Phys. Rev. C* **84**, 054916 (2011), [arXiv:1105.3719 \[hep-ph\]](#).
- [37] Y. Cai, T. D. Cohen, B. A. Gelman, and Y. Yamauchi, *Phys. Rev. C* **100**, 024911 (2019), [arXiv:1905.02753 \[nucl-th\]](#).
- [38] A. Schwarzschild and C. Zupancic, *Phys. Rev.* **129**, 854 (1963).
- [39] H. Sato and K. Yazaki, *Phys. Lett. B* **98**, 153 (1981).
- [40] R. Mattiello, A. Jahns, H. Sorge, H. Stöcker, and W. Greiner, *Phys. Rev. Lett.* **74**, 2180 (1995).
- [41] J. L. Nagle, B. S. Kumar, D. Kusnezov, H. Sorge, and R. Mattiello, *Phys. Rev. C* **53**, 367 (1996).
- [42] R. Mattiello, H. Sorge, H. Stöcker, and W. Greiner, *Phys. Rev. C* **55**, 1443 (1997), [arXiv:nucl-th/9607003](#).
- [43] A. Polleri, J. P. Bondorf, and I. N. Mishustin, *Phys. Lett. B* **419**, 19 (1998), [arXiv:nucl-th/9711011](#).
- [44] R. Scheibl and U. W. Heinz, *Phys. Rev. C* **59**, 1585 (1999), [arXiv:nucl-th/9809092](#).
- [45] N. Sharma, T. Perez, A. Castro, L. Kumar, and C. Nattrass, *Phys. Rev. C* **98**, 014914 (2018), [arXiv:1803.02313 \[hep-ph\]](#).
- [46] W. Zhao, L. Zhu, H. Zheng, C. M. Ko, and H. Song, *Phys. Rev. C* **98**, 054905 (2018), [arXiv:1807.02813 \[nucl-th\]](#).
- [47] X.-Y. Zhao, Y.-T. Feng, F.-L. Shao, R.-Q. Wang, and J. Song, *Phys. Rev. C* **105**, 054908 (2022), [arXiv:2201.10354 \[hep-ph\]](#).
- [48] R.-Q. Wang, J.-P. Lv, Y.-H. Li, J. Song, and F.-L. Shao, *Chin. Phys. C* **48**, 053112 (2024), [arXiv:2210.10271 \[hep-ph\]](#).
- [49] R.-Q. Wang, F.-L. Shao, and J. Song, *Phys. Rev. C* **103**, 064908 (2021), [arXiv:2007.05745 \[hep-ph\]](#).
- [50] R.-Q. Wang, Y.-H. Li, J. Song, and F.-L. Shao, *Phys. Rev. C* **109**, 034907 (2024), [arXiv:2309.16296 \[nucl-th\]](#).
- [51] S. Acharya *et al.* (ALICE), (2024), [arXiv:2405.19839 \[nucl-ex\]](#).
- [52] L.-W. Chen, C. M. Ko, and B.-A. Li, *Nucl. Phys. A* **729**, 809 (2003), [arXiv:nucl-th/0306032](#).
- [53] L. Zhu, C. M. Ko, and X. Yin, *Phys. Rev. C* **92**, 064911 (2015), [arXiv:1510.03568 \[nucl-th\]](#).
- [54] S. Mrowczynski, *Acta Phys. Polon. B* **48**, 707 (2017), [arXiv:1607.02267 \[nucl-th\]](#).
- [55] A. Kisiel, W. Florkowski, and W. Broniowski, *Phys. Rev. C* **73**, 064902 (2006), [arXiv:nucl-th/0602039](#).
- [56] C. Alt *et al.* (NA49), *Phys. Lett. B* **685**, 41 (2010), [arXiv:0809.1445 \[nucl-ex\]](#).
- [57] I. Angeli and K. P. Marinova, *Atom. Data Nucl. Data Tabl.* **99**, 69 (2013).
- [58] M. Puccio, CERN-THESIS-2017-338, Ph.D. thesis, Turin U. (2017).
- [59] J. Adam *et al.* (ALICE), *Phys. Rev. C* **93**, 024905 (2016), [arXiv:1507.06842 \[nucl-ex\]](#).
- [60] P. Chakraborty, A. K. Pandey, and S. Dash, *Eur. Phys. J. A* **57**, 338 (2021), [arXiv:2010.12161 \[hep-ph\]](#).
- [61] J. Adams *et al.* (STAR), *Phys. Rev. C* **71**, 044906 (2005), [arXiv:nucl-ex/0411036](#).
- [62] S. Acharya *et al.* (ALICE), *Phys. Rev. C* **101**, 044907 (2020), [arXiv:1910.07678 \[nucl-ex\]](#).
- [63] D. Oliinychenko, L.-G. Pang, H. Elfner, and V. Koch, *Phys. Rev. C* **99**, 044907 (2019), [arXiv:1809.03071 \[hep-ph\]](#).
- [64] D. Oliinychenko, L.-G. Pang, H. Elfner, and V. Koch, *MDPI Proc.* **10**, 6 (2019), [arXiv:1812.06225 \[hep-ph\]](#).
- [65] Y. Bailung, N. Shah, and A. Roy, *Nucl. Phys. A* **1037**, 122701 (2023).
- [66] F.-X. Liu, Z.-L. She, H.-G. Xu, D.-M. Zhou, G. Chen, and B.-H. Sa, *Sci. Rep.* **12**, 1772 (2022).
- [67] E. Schnedermann, J. Sollfrank, and U. W. Heinz, *Phys. Rev. C* **48**, 2462 (1993), [arXiv:nucl-th/9307020](#).
- [68] J. Adam *et al.* (ALICE), *Phys. Rev. C* **93**, 024917 (2016), [arXiv:1506.08951 \[nucl-ex\]](#).
- [69] K.-J. Sun, C. M. Ko, and B. Dönigus, *Phys. Lett. B* **792**, 132 (2019), [arXiv:1812.05175 \[nucl-th\]](#).
- [70] P. Kalinak (ALICE), *PoS EPS-HEP2017*, 168 (2017).
- [71] W.-b. Chang, R.-q. Wang, J. Song, F.-l. Shao, Q. Wang, and Z.-t. Liang, *Symmetry* **15**, 400 (2023), [arXiv:2302.07546 \[nucl-th\]](#).
- [72] C. A. Bertulani, *Phys. Lett. B* **837**, 137639 (2023), [arXiv:2211.12643 \[nucl-th\]](#).
- [73] D.-N. Liu, C. M. Ko, Y.-G. Ma, F. Mazzaschi, M. Puccio, Q.-Y. Shou, K.-J. Sun, and Y.-Z. Wang, *Phys. Lett. B* **855**, 138855 (2024), [arXiv:2404.02701 \[nucl-th\]](#).
- [74] H. Clement, *Prog. Part. Nucl. Phys.* **93**, 195 (2017), [arXiv:1610.05591 \[nucl-ex\]](#).
- [75] T. Iritani *et al.* (HAL QCD), *Phys. Lett. B* **792**, 284 (2019), [arXiv:1810.03416 \[hep-lat\]](#).
- [76] S. Zhang and Y.-G. Ma, *Phys. Lett. B* **811**, 135867 (2020), [arXiv:2007.11170 \[hep-ph\]](#).
- [77] H. Garcilazo and A. Valcarce, *Phys. Rev. C* **99**, 014001 (2019), [arXiv:1901.05678 \[hep-ph\]](#).
- [78] L. Zhang, S. Zhang, and Y.-G. Ma, *Eur. Phys. J. C* **82**, 416 (2022), [arXiv:2112.02766 \[hep-ph\]](#).